Chapter 6

In-situ experiments and high fidelity simulations

As mentioned throughout this work, components obtained by additive manufacturing present fabrication defects, such as surface roughness, layer discontinuities, or internal porosity, that strongly affect their mechanical performance.

The use of numerical simulations is very useful for studying how fabrication defects influence the mechanical behavior of lattice materials. As described in sections 3.1 and 5.2.2.3, computational homogenization based on the fast Fourier transform (FFT) allows for highly efficient numerical simulations without the need for a mesh, reducing computational resources (Lucarini and Segurado, 2019; Lucarini, Upadhyay, and Segurado, 2021; Lucarini et al., 2022). With this technique, it is possible to directly use reconstructions obtained from X-ray tomography (Lucarini et al., 2022), which include the internal structure. Moreover, these models can be used to simulate the mechanical tests performed on the same exact specimens, allowing the analysis of the stress distribution and effect of defects (Lucarini et al., 2022).

In this chapter, the experimental analysis of Polyamide12 individual cells and struts is integrated with numerical simulations to analyze how defects influence the mechanical behavior and fracture of these materials and also the non linear behavior. In-situ tests of unit cells and single struts of different diameters have been conducted using X-ray tomography. These tests allowed the observation of how cracks nucleate and how damage propagates during the experiments. From the reconstructions of the tomograms, exact digital replicas of the sample volumes were created and used to simulate the tests using an FFT-based method considering a phase-field fracture model to predict the behavior and further investigate crack nucleation. Additionally, the non-linear mechanical behavior was studied using a viscoelastic-viscoplastic (VEVP) model, which was first calibrated to obtain fitted parameters and then used to generate results.

6.1 Experimental results from in-situ tests

In-situ tests were carried out in unit cells and single struts under two different experimental set-ups in two different tomographs, one for compression of the unit cells and the other for tensile tests of the struts.

6.1.1 Experimental set-up

Two experimental set-ups were used; one designed for tensile tests and the other for compression tests.

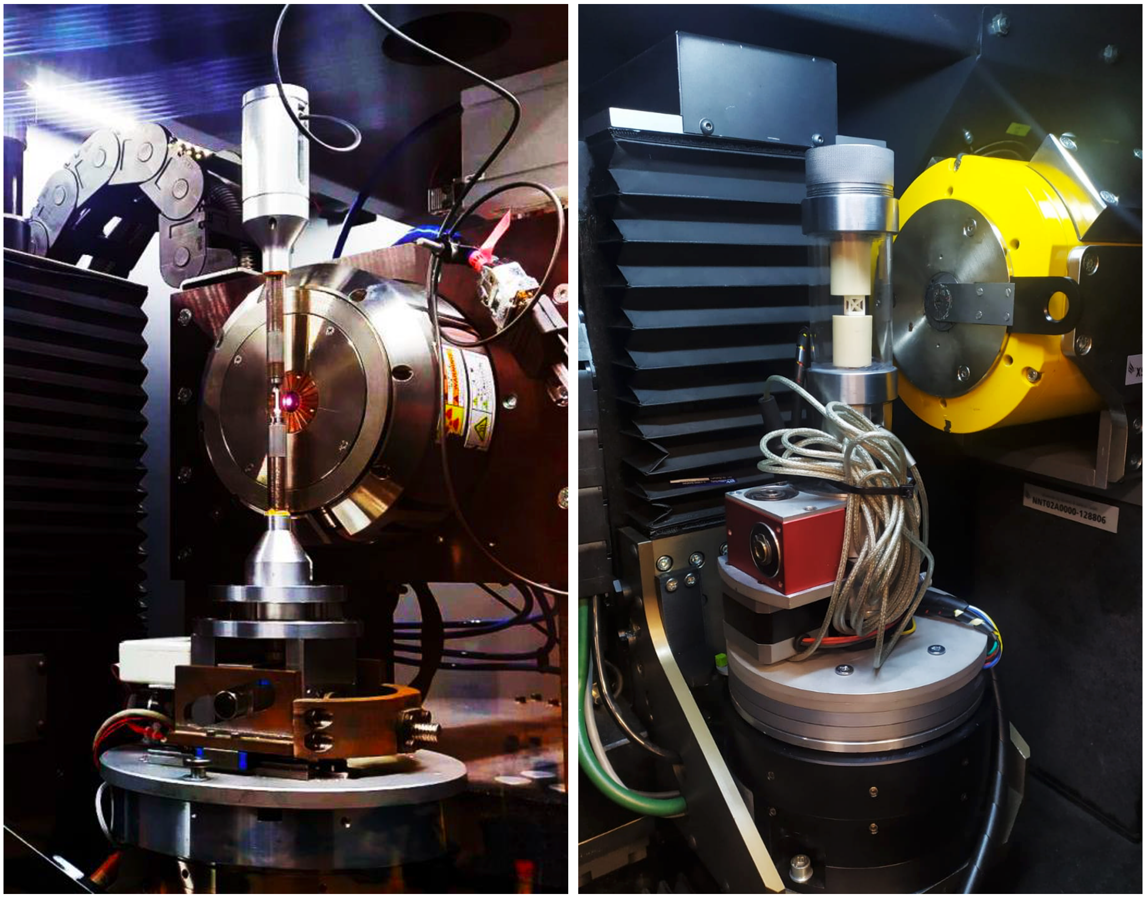

(a) **(b)**

Figure 6.1: In-situ experimental setup for (a) tensile tests on the struts and (b) compression tests on the BCC unit cells.

Single struts in-situ tensile tests

Cylindrical tensile specimens with diameters of 0.7, 1.0, and 1.5 mm and a length of 6 mm were fabricated, mimicking the geometries of the individual struts, as it was done in section 5.1.3. These specimens were printed in three different directions, resulting in samples with layers oriented perpendicular, parallel, and oblique to the load. These printing directions are H, V, and T, respectively.

The samples were scanned in the *MatéIS* facilities at INSA Lyon using the *RX Solutions EasyTom Nano* tomograph, with a voxel size of 4 µm, a voltage of 80 kV, and a current of 80 µA, without the need of using a filter to reduce the electron beam hardening effect. A non-commercial in-situ tensile machine equipped with a 1.5 kN load cell was used to perform tensile tests. The tensile process was displacement-controlled, with a speed of 0.0139 mm/s ($2.78 \times 10^{-3}\ s^{-1}$). Figure 6.1a shows the configuration of the in-situ tests.

To study the evolution of the microstructure with damage, the tests were carried out stepwise, allowing the tomography of the sample to be performed at different deformation stages until fracture. At each step, the sample was slightly unloaded to prevent relaxation movements or crack propagation. Tomographies were taken when the sample entered the non-linear regime to observe microstructural changes due to damage. Additionally, to study deformation and determine whether the non-linear region was due to damage or plasticity, an in-situ test was performed in 20 steps, applying DVC (Digital Volume Correlation). For DVC, an in-house code developed at INSA Lyon was used. Each step consisted of increasing the displacement by 58 µm in tension, and to avoid stress relaxation during tomography, the sample was compressed by 10 µm. Therefore, each tomography was taken at every 48 µm of displacement. In this case, the voxel size was 8 µm.

The tomographies of all tests and steps were converted into RVEs of $\approx 256^3$ voxels with a resolution of 36.3 µm/pixel following the process mentioned in 3.3.1 for the simulations.

Unit cells in-situ compression tests

Unit cells with strut diameters of 0.7 and 1.0 were subjected to in-situ compression tests. The samples were scanned *IMDEA Materials* using the *GE (Phoenix) Nanotom 160 kV* tomograph, with a voxel size of 8 µm, a voltage of 130 kV, and a current of 80 µA, without the need to use a filter to reduce the electron beam hardening effect. A non-commercial in-situ compression machine equipped with a *FUTEK IPM650* controller and a 200 N load cell was used. The compression process was displacement-controlled, with the strain rates shown in Table 6.1 for each unit cell size. Figure 6.1b shows the configuration of the compression in-situ tests.

Table 6.1: Strain rate and displacement for each step of the in-situ compression tests of unit cells with 0.7 and 1.0 mm struts diameter.

	Unit cells	
Strut diameter [mm]	**0.7**	**1.0**
$\dot{\varepsilon}\ [s^{-1}]$	5.19×10^{-4}	3.91×10^{-4}
Step displacement [µm]	195	260

To study the evolution of the microstructure with damage, the tests were carried out stepwise, allowing the tomography of the sample to be performed at different deformation stages until 20 % of deformation. In Table 6.1, the displacement applied at each step for both unit cell sizes is reported. Also, in this case, after each step, the sample was slightly unloaded to prevent relaxation movements or crack propagation.

As with struts, the tomographies were converted into RVEs of $\approx 256^3$ voxels with a resolution of 36.3 µm/pixel following the process mentioned in 3.3.1 for the simulations.

6.1.2 Experimental results of struts

Figure 6.2 shows the force-displacement curves obtained from the in-situ tests. A significant variation in mechanical behavior can be observed among the different samples printed with the same diameter but in different directions. Despite the lack of repeatability, all samples exhibit both a linear and a non-linear regime. The non-linearity is likely due to the evolution of damage experienced by the sample, given the limited plasticity it exhibits after fracture. Additionally, the unloading steps taken throughout the test to capture the tomographies are evident. In the 0.7 mm diameter sample printed in the T direction, radiographs were taken instead of tomographies, so the unloadings were unnecessary. The curve for the sample used for DVC is not shown in Figure 6.2.

The high variability in results is due to two main reasons. First, the printing parameters are not optimal for manufacturing struts with sub-millimeter diameters, leading to a strong surface roughness. Also, the fabrication defects are unique to each sample, influencing each one differently.

In order to obtain a realistic stress-strain response from the tests, it is necessary to perform a direct measurement of strain because, due to the testing machine's low stiffness, the carriage's movement cannot be directly associated with the displacement of the sample's effective length. The use of extensometers is also not possible here because of the small sample size. For this reason, it was only possible to obtain the stress-strain curve from the test conducted for DVC. Therefore, the experimental results in Fig. 6.2 have not been used for mechanical property characterization because of the limitations in strain measurement and the limited number of tests performed per sample type. Instead, the focus has been solely on studying the evolution of the microstructure as it relates to damage.

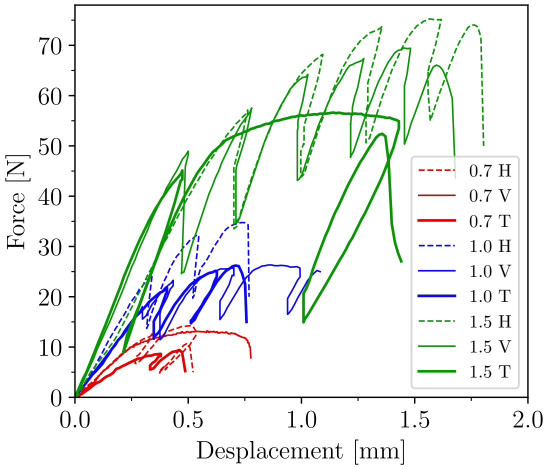

Figure 6.2: Experimental force-displacement curves from single strut in-situ tests with X-ray tomography.

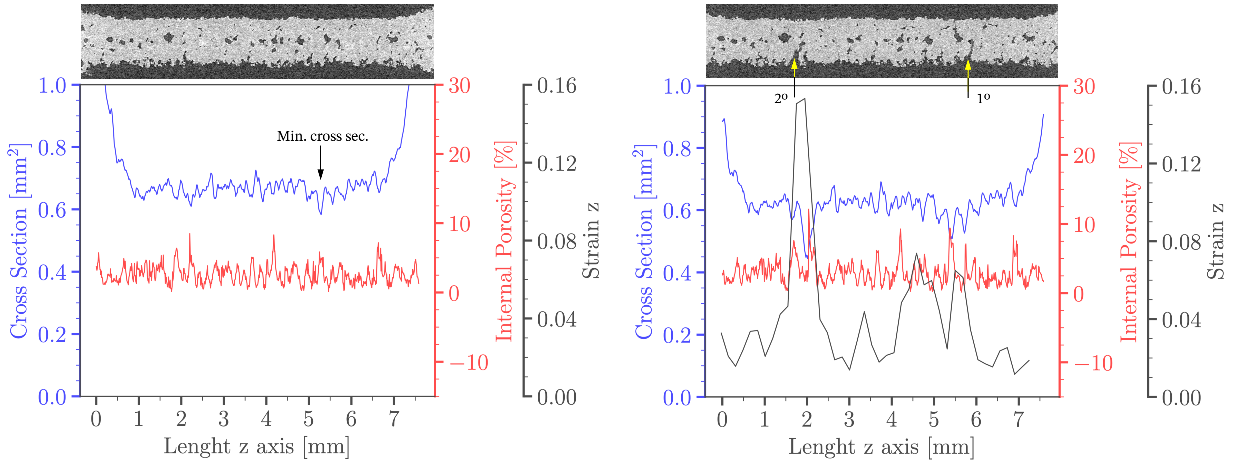

(a) **(b)**

Figure 6.3: Analysis of strut tested with DVC in (a) the initial state and (b) the step before failure.

Figure 6.3 depicts the sample used for DVC, with a diameter of 1 mm, printed in the T direction. In this sample, the first crack to nucleate, located at the right end, coincides with the area of the smallest cross-section. However, failure occurs due to the propagation of a second crack, which nucleates at later stages of deformation and is located near the region with the highest initial porosity. Additionally, the local deformations obtained through DVC are shown in black, revealing a high concentration of localized deformation in the fracture zones.

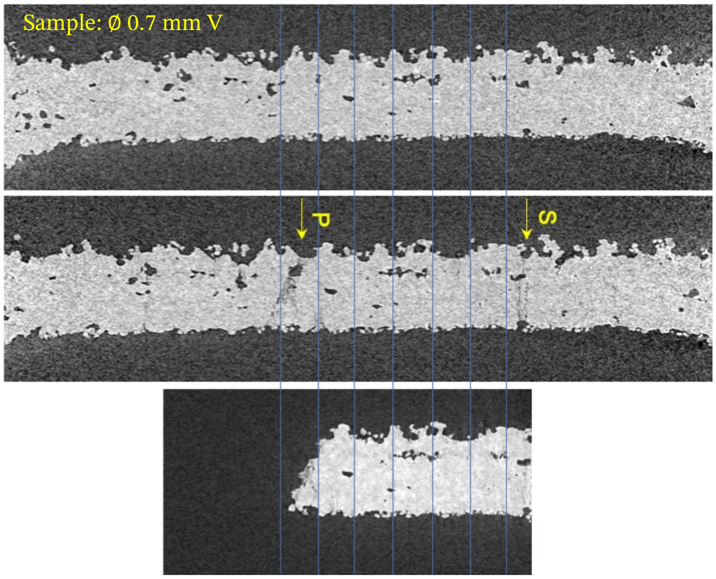

Figure 6.4: Single strut of 1.0 mm diameter with layers in the V direction. S indicates a crack originated in the surface, and P indicates a crack originated in an internal pore.

In Figure 6.4, three different states of a 1 mm diameter sample printed in the V direction are shown. In the upper figure, the sample is in its initial state before applying any load. In the middle image, an intermediate stage is represented where the sample shows two cracks, one originating at the surface (S) and the other from an internal pore (P). The bottom image represent the final stage after failure, showing the fracture plane, which, in this case, resulted from the propagation of the crack that originated at the pore.

From the tomographies obtained during the in-situ tests, it can be observed that cracks predominantly nucleate at the surface, with fewer nucleations originating from internal defects, as seen in Figures 6.3b and 6.4. Additionally, many cracks nucleate in regions corresponding to the smallest cross-section in the initial state, as occurs in Figure 6.3. However, cracks do not always nucleate in areas of higher porosity. The propagation of cracks mainly depends on the printing direction. After fracture, plasticity is only observed in the area close to the failure site, as illustrated in Figure 6.4. There is no direct correlation between failure due to a crack originating at the surface or from internal pores, nor is there a consistent pattern regarding cracks originating in regions of the smallest cross-section.

6.1.3 Experimental results of unit cells

Figure 6.5 shows the stress-strain curves obtained from the in-situ tests of the unit cells with 0.7 and 1.0 mm diameter struts with as-built surface condition and surface-treated condition. The curves present similar shapes and values to those obtained from the characterization experiments shown in section 5.1.2 and Figure 5.1b. Compared to the tests carried out for mechanical characterization, where there was no significative improvement in the performance of cells with diameters higher than 0.5 mm, the surface-treated samples performed better than the non-treated ones during in-situ tests, as the samples reached higher maximum stresses, especially on the cell with 0.7 mm diameter strut. The variations observed between the curves obtained from the different tests can be attributed to multiple factors, such as the different strain rates the tests have been carried out, environmental conditions inside and outside the tomograph, and sample age, among others. In addition, the observations from the mechanical behavior obtained from the in-situ tests come from one sample for each geometry and surface treatment. In contrast, the observations in section 5.1.2 were done on multiple samples. For this reason, the observations from the in-situ stress-strain curves cannot be used to study the mechanical behavior of these samples.

In contrast to the struts, where there is no correlation between the type of defect and the location of the crack nucleation, in unit cells, crack nucleation is strongly related to the geometrical features of the samples. The first cracks always nucleate before 10 % of strain in the inner parts of the nodes that join the vertical struts with the diagonal ones and propagate with an angle of 45° with respect to the load direction, as observed in Figure 6.6. In addition, secondary cracks appear in the middle of the vertical struts, approximately at 20 % of strain only in the non-surface treated samples. This crack nucleation behavior has also been observed in the unit cells during the tests explained in section 5.1.2.

Although surface treatment does not cause significant improvements in the mechanical behavior of struts, it reduces the nucleation sites in the surface of the struts as it reduces the surface defects, which act as local stress concentration sites (Serrano-Munoz et al., 2017).

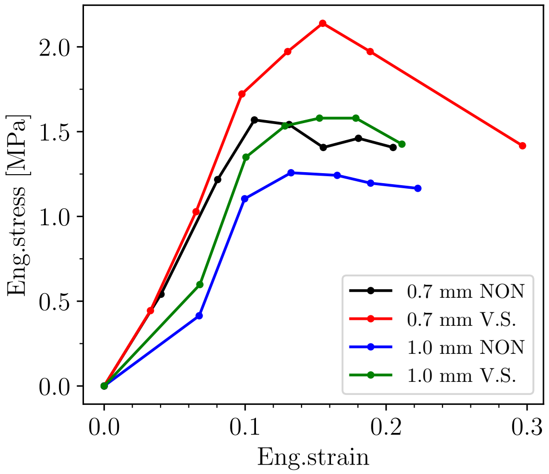

Figure 6.5: Stress strain curves of unit cells from X-ray in-situ tests.

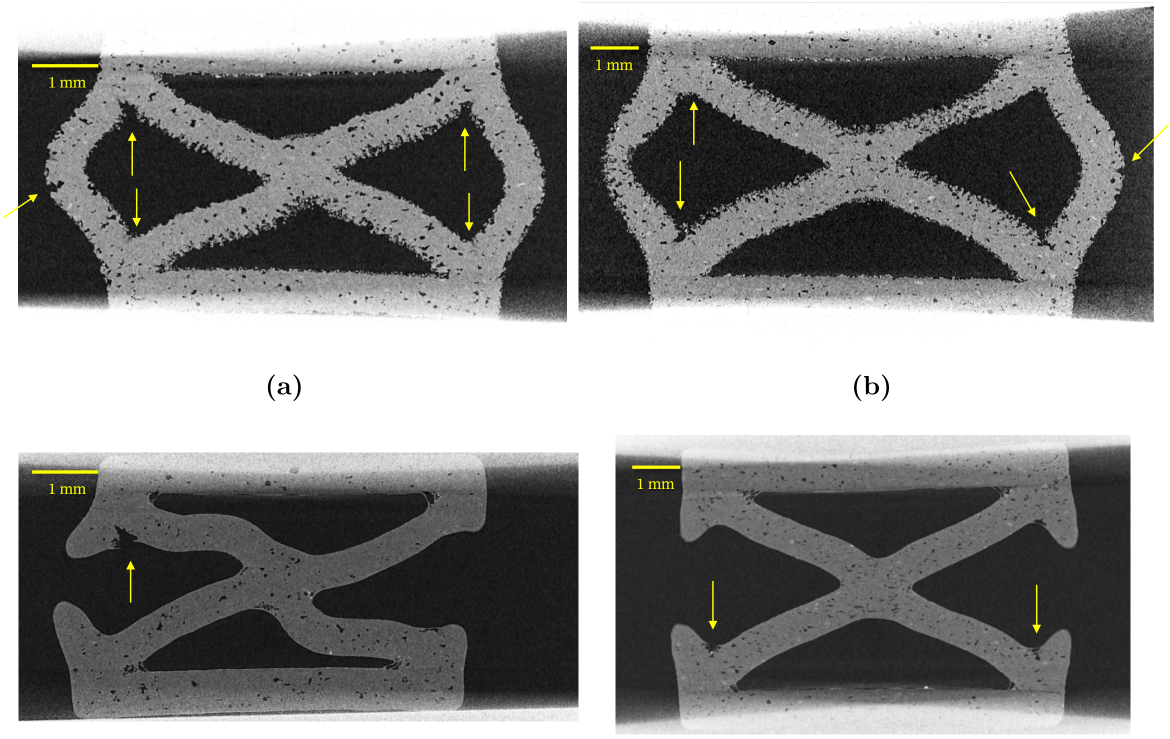

(a)

(b)

(c)

(d)

Figure 6.6: Cross section from the final step of in-situ tests with X-ray tomography of unit cells with (a) 0.7 mm diameter struts without surface treatment, (b) 1.0 mm diameter struts without surface treatment, (c) 0.7 mm diameter struts with surface treatment, and (d) 1.0 mm diameter struts with surface treatment.

6.2 Linear elastic-fracture simulations

6.2.1 Struts

The simulation of the tests was performed using the phase field fracture model presented in section 3.4. The pristine material follows a linear elastic model with values of 1.7 GPa for E and 0.4 for ν. Fracture energy values of 250, 500, and 1500 N/m, along with characteristic lengths (l_{car}) of 90, 180, 600, and 1800 µm, have been used. In Figure 6.7b, a cross-sectional view of a representative volume obtained from the raw tomography (Figure 6.7a) is shown, where internal defects can be observed. In addition to the simulation of the tests with the actual geometry obtained from X-rays, another set of simulations was conducted in which internal porosity was removed, Figure 6.7c. This set of simulations was performed to study the influence of surface roughness on crack nucleation and propagation uncoupled to the effect of internal porosity.

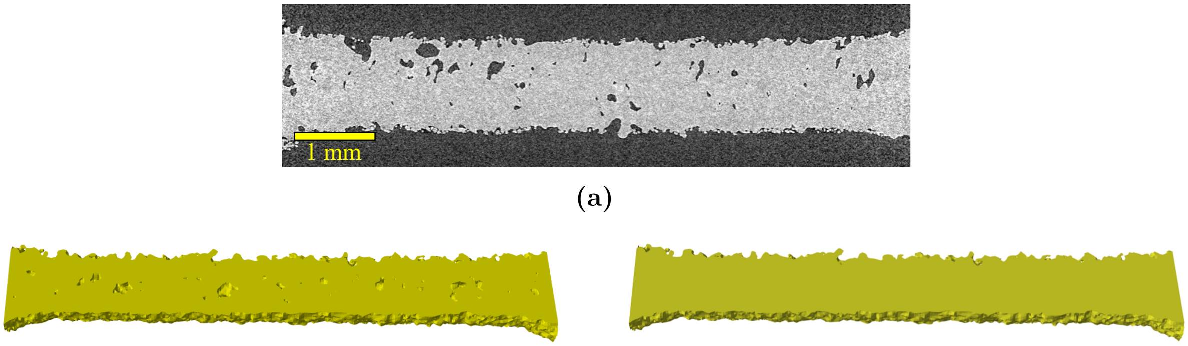

(a)

(b)

(c)

Figure 6.7: Tomographic volume of 1 mm strut printed in oblique direction used for porosity analysis and diameter measurements where (a) raw gray-scale tomography slice, (b) reconstruction from original tomography including defects, and (c) reconstruction with no pores. The reconstructed volume is virtually cut in the middle of the sample for this figure.

Simulations have been conducted with different values to define the fracture model, specifically the parameters G_c and l_{car}. These parameters determine the shape of the predicted force-displacement curves. Although no pair of values accurately represents the experimental force-displacement curves, the values of $G_c = 1500$ N/m and $l_{car} = 600$ µm best align with the test results. Simulations are performed for the actual microstructure obtained in the tomographies and also for artificial microstructures in which internal porosity has been removed.

Figure 6.8 presents the stress-strain curves for the sample used in DVC. In the figure, the experimental curve is represented together with the curves obtained from simulations with various values of the parameters l_{car} and G_c. The curves obtained using the representative volumes without porosity reached higher maximum loads than their corresponding microstructures with porosity; however, their behaviors are similar. For this reason, only the result of a single simulation using a microstructure with porosity is represented in the figure, using grey color.

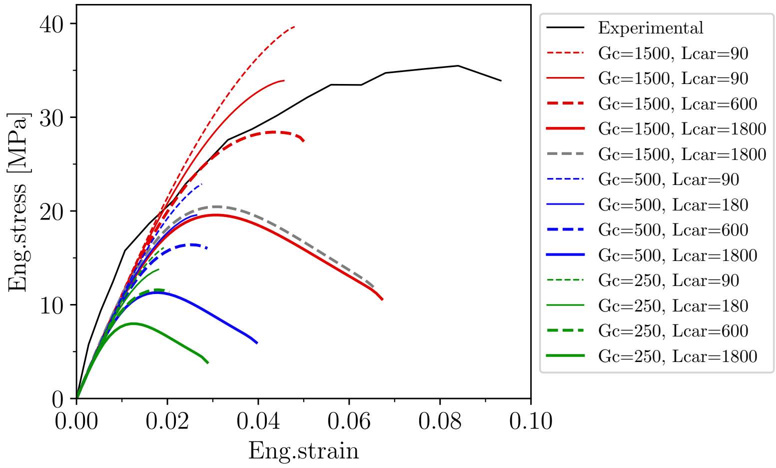

Figure 6.8: Stress-strain curves from the experimental DVC test and predictions using PFF with different parameters.

Figure 6.9: Sample used for DVC. Up: RVE with pores, Middle: fracture prediction using RVE with pores, and Down: fracture prediction using RVE without pores. Where sdv1 indicates the damage phase field.

It has been observed that the behavior obtained by the simulation of this DVC experiment is influenced more by surface roughness than by internal porosity. As the fracture energy decreases, the maximum damage is reached at lower levels of strain and stress. On the contrary, with increasing l_{car}, the material exhibits a more ductile behavior before fracture due to the extension of the non-linear region. However, as l_{car} increases, the maximum stress the material can achieve decreases.

In addition to the force-displacement results, the simulations allow for the localization of damage within the specimen and the formation or propagation of critical cracks (Figure

6.9). Generally, the simulations predict the locations where damage is concentrated, but they do not always accurately predict which crack propagates to cause the final failure. The simulations typically show a single propagating crack, which often coincides with the first crack nucleated during the test. However, in experiments, failure does not always occur due to the propagation of the first nucleated crack. In Figure 6.3, it can be seen that the first crack nucleated at the location of the smallest effective area aligns with the crack propagation location in the simulation shown in Figure 6.9.

In some cases, despite the parameter variation, the crack consistently appears in the same section, indicating a clear stress concentration in those areas, as seen in Figure 6.9. However, even if the crack forms in the same position, it may not align with the experimental fracture. In other cases, changes in the parameters do affect the prediction of the crack localization, making it coincide with the experimental results, as shown in Figure 6.10.

Figure 6.10 compares the location of experimental cracks with predictions made using different parameters and representative volumes from a 1.5 mm diameter sample printed in the T direction. This sample has a different diameter than the one shown in Figure 6.9.

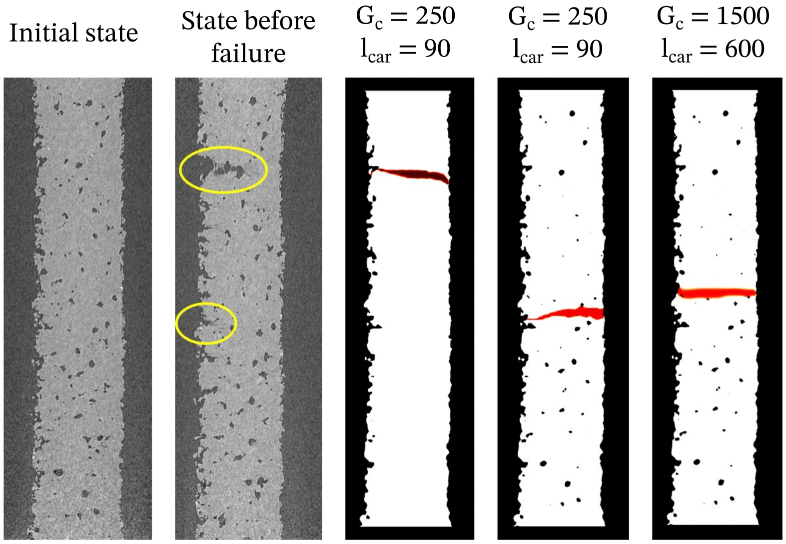

Figure 6.10: Strut of 1.5 mm diameter with layers in T direction showing raw tomographies of the initial and before failure states, and the fracture predictions using different parameters.

To analyze whether the resulting crack is influenced by internal porosity, new models have been generated in which the internal porosity has been removed. The simulation results are presented in Figures 6.9 alongside the results from the original microstructure. These porosity-free simulations provide insight into which samples fail due to cracks nucleated at the surface.

In summary, it can be stated that the brittle fracture approach using phase field and real microstructures does not always predict failure in a consistent manner with experiments. The differences are probably due to the use of linear elastic fracture, which does not accurately represent the actual degradation in the material. The type of fracture observed and the force-displacement curves suggest a cohesive crack behavior with a maximum strength characterizing the nucleation of cracks in high-stress regions. Furthermore, the behavior of monolithic Polyamide 12 in the absence of failure is not elastic, indicating that a material model considering viscoelasticity and viscoplasticity would be more appropriate, as observed in the mechanical characterization of bulk and struts in sections 4.1 and 5.1.3, respectively (Cobian et al., 2022).

6.2.2 Unit cells

In the case of unit cells, the simulations consistently predicted the damage at the nodes, where cracks appear in the experiments in the in-situ and conventional compression tests, as shown in Figure 6.11. However, the simulations were challenging as there were convergence issues when the strains were over 8 % for the defect-free RVE and memory and simulation times for the RVEs obtained from tomographies.

These difficulties originate from the suboptimal adaptation of FFTMAD with phase-field fracture implemented for lattice structures and a material consecutive model that does not adapt to the real materials behavior, as mentioned in the previous section, with the prediction of the strut's crack nucleation and propagation behavior. These difficulties have prevented the successful generation of stress-strain curves from comparing them with the experimental ones, and it also was not possible to complete simulations with RVEs obtained from tomographies.

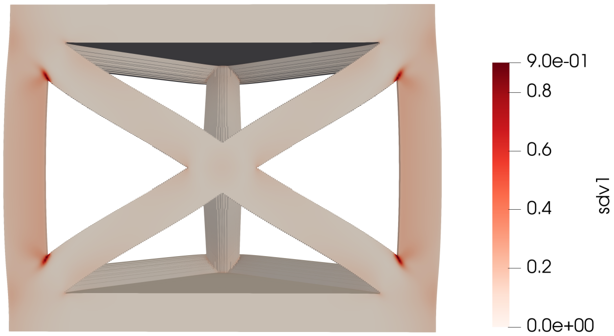

Figure 6.11: Damage prediction on the as-designed BCC unit cell RVE. Where sdv1 indicates the damage phase field.

6.3 Elasto-visco plastic simulations

Experimental mechanical tests (see Figures 5.1b and 5.2) show that unit cells and struts present not only an elastic regime but also a strain rate-dependent plastic regime, where the yield point increases with the strain rate, showing viscoplasticity. In addition, the strains reached until failure surpasses 10 %, overcoming large deformations. Up til now, all the simulations have been done with a linear elastic model, which, although it has given information about the influence of porosity, can only predict the effective elastic modulus, as seen in section 5.2.2.3. In addition, in section 6.1.2, the predictions with phase-field fracture deviate from the experimental results because this material model did not represent the actual degradation of the material as a model considering viscoelasticity and viscoplasticity would be more appropriate.

For this reason, the finite strain VEVP material model introduced in section 3.5, which was calibrated at both the macroscopic and microscopic scales using experimental data, was used to predict the non-linear response of the struts and unit cells.

6.3.1 Model calibration

The experimental data obtained from the mechanical tests shown in chapter 4 and summarized in Table 6.2 for the bulk material and section 5 for the single struts were used to fit the material parameters of the finite-strains visco-elastic visco-plastic material model using BI. The single struts were tested only under tensile uniaxial loading at strain rates of 2.78×10^{-3}, 1.67×10^{-2}, 1.67×10^{-1}, and 1.67 s^{-1}.

For the fitting process, the number of Maxwell branches is set to $N = 8$ (equations 3.14 and 3.15) based on the observations made during the experimental tests. The material parameters $\boldsymbol{\vartheta}$ are divided into the viscoelastic parameters $\boldsymbol{\vartheta}^{\boldsymbol{ve}}$ and the viscoplastic parameters $\boldsymbol{\vartheta}^{vp}$ which are explained in the next paragraph. Using the Markov Chain Monte Carlo (MCMC) algorithm, the parameters are inferred by choosing random variables between a range of values. Due to the lack of compression tests on single struts, the compression macroscopic parameters are used on the microscopic scale. Then, using maximum a posteriori (MAP), the fitted parameters for the VEVP model that produce the most similar stress-strain curves to the experimental ones are selected. The comparison between the experimental data and predicted curves is shown later in Figure 6.13 of section 6.3.

Table 6.2: Bulk material loading conditions used for BI

Loading speed	experiment type	Strain rate $\dot{\varepsilon}[s^{-1}]$
Low	Tension	7.37×10^{-4}
		7.37×10^{-3}
		7.37×10^{-2}
	Compression	2.78×10^{-3}
		2.78×10^{-2}
		2.78×10^{-1}
Medium	Compression	1.0
		10.0
High	Compression	160.0
		380.0
		640.0
		750.0
		890.0
Relaxation (compression)	Elastic loading	7.37×10^{-3}
	Elasto-plastic loading	7.37×10^{-3}

Viscoelastic parameters

The Young's modulus E_∞, Poisson's ration ν_∞, Bulk moduli K_i, Shear moduli G_i, and volumetric k_i and deviatoric g_i retardation times conform the $\boldsymbol{\vartheta}^{ve}$ parameters to be inferred.

The relaxation times (see equations 3.16 and 3.17) g_1 and k_1 are chosen to be random retardation variables to be inferred, and the rest corresponding to the branches $i = 2$, ..., 8 are defined as $g_i = g_1 \times 10^{-(i-1)}$ and $k_i = k_1 \times 10^{-(i-1)}$. In addition, G_i and K_i, when $i = 1, ..., 8$, are defined as random variables to be inferred as $E(t)$ and $\nu(t)$ are both time-dependent in polymer materials. Equilibrium moduli G_∞ and K_∞ are constants defined in eq. 6.1. The ranges of the parameters are defined using rough estimation ranges based on the experimental results and literature. The values of G_i, g_i, K_i, and k_i present ranges that include several orders of magnitude, and to make them have the same probability during the random walks, their log_{10} values are used as the uniformly distributed random variables. The ranges chosen for each viscoelastic parameter and the fitted parameters are shown in Tables 6.3 and 6.4, respectively.

$$G_\infty = \frac{E_\infty}{2(1+\nu_\infty)} \text{ and } K_\infty = \frac{E_\infty}{3(1-2\nu_\infty)} \tag{6.1}$$

Table 6.3: Uniform distribution ranges of the viscoelastic material parameters. Where $i = 1, ..., 8$, the units of G_i and K_i are MPa, and g_1 and k_1 are s.

$\boldsymbol{\vartheta}^{ve}$	E_∞ [MPa]	ν_∞	$log_{10}G_i$	$log_{10}K_i$	$log_{10}g_1$	$log_{10}k_1$
Ranges macro	[800 - 1600]	[0.20 - 0.45]	[-1.0 - 4.5]		[0.0 - 3.0]	
Ranges micro	[200 - 1600]	0.283	[-1.0 - 4.5]		[0.0 - 3.0]	

Table 6.4: Viscoelastic material parameters for the macro and micro scale obtained with Bayesian inference fitting after using MAP.

$\boldsymbol{\vartheta}^{ve}$	E_∞ [MPa]	ν_∞	$log_{10}g_1$	$log_{10}k_1$
Params macro	1374.3	0.283	0.897	1.035
Params micro	622.8	0.283	0.540	1.888

$\boldsymbol{\vartheta}^{ve}$	$log_{10}K_1$	$log_{10}K_2$	$log_{10}K_3$	$log_{10}K_4$	$log_{10}K_5$	$log_{10}K_6$	$log_{10}K_7$	$log_{10}K_8$
Params macro	4.220	-0.236	2.956	2.113	-0.078	-3.898	1.708	3.146
Params micro	2.322	3.112	2.386	-0.233	1.767	0.614	2.360	3.231

$\boldsymbol{\vartheta}^{ve}$	$log_{10}G_1$	$log_{10}G_2$	$log_{10}G_3$	$log_{10}G_4$	$log_{10}G_5$	$log_{10}G_6$	$log_{10}G_7$	$log_{10}G_8$
Params macro	-0.066	1.066	0.885	0.390	1.334	0.815	3.182	0.953
Params micro	-0.368	-0.714	0.827	0.078	1.707	-0.522	1.410	3.039

Viscoplastic parameters

The set $\boldsymbol{\vartheta^{vp}}$ is composed of 12 parameters that have to be identified; the viscosity η and rate sensitivity exponent s defined in eq. 3.19, the yield parameter α of eq. 3.20, the initial compressive yield stress σ_c^0 computed in eq. 3.21 and tensile yield stress σ_t^0 through m^0, the parameter β related to the plastic Poisson ratio in eq. 3.23, and hardening parameters c_0, H_c^0 h_t of the compressive regime (eq. 3.24) and tensile regime t_0, H_t^0 h_t (eq. 3.25). As with $\boldsymbol{\vartheta^{ve}}$, the parameters to be identified adopt random values within a range, and in the case of η, c_0, H_c^0, t_0 and H_c^0 their logarithms (log_{10}) are applied. Tables 6.5 and 6.6 show the ranges chosen and the values obtained for each viscoplastic parameter, respectively.

Table 6.5: Uniform distribution ranges of the viscoplastic material parameters for the macroscale (bulk level) and the microscale (strut level). Where η is in MPa · s, and t_0, c_0, H_t^0 and H_c^0 are in MPa.

$\boldsymbol{\vartheta^{vp}}$	$log_{10}\eta$	s	α	β	σ_c^0 [MPa]	m^0
Ranges macro	[3.0 - 5.3]	[0.01 - 0.5]	[1.0 - 7.0]	[0.0 - 2.0]	[5.0 - 60.0]	[0.1 - 0.9]
Ranges micro	[3.0 - 5.3]	[0.01 - 2.0]	3.705	0.2175	[20.0 - 35.0]	0.777

$\boldsymbol{\vartheta^{vp}}$	$log_{10}t_0$	$log_{10}c_0$	$log_{10}H_t^0$	$log_{10}H_c^0$	h_t	h_c
Ranges macro	[-5.0 - 3.0]		[-3.0 - 2.0]		[0 - 10000]	
Ranges micro	[5.0 - 3.0]	[-3.0 - 0.0]	[-5.0 - 2.0]	[0.0 - 2.0]	[0 - 10000]	[200 - 1000]

Table 6.6: Viscoplastic material parameters for the macro and micro scale obtained with Bayesian inference fitting after using MAP.

$\boldsymbol{\vartheta^{vp}}$	$log_{10}\eta$	s	α	β	σ_c^0 [MPa]	m^0
Params macro	5.183	0.179	3.705	0.2175	29.696	0.777
Params micro	3.173	0.298	3.705	0.2175	34.882	0.777

$\boldsymbol{\vartheta^{vp}}$	$log_{10}t_0$	$log_{10}c_0$	$log_{10}H_t^0$	$log_{10}H_c^0$	h_t	h_c
Params macro	2.145	-2.533	-3.184	1.157	9648.948	299.094
Params micro	2.276	-2.888	-2.091	0.907	9475.703	236.011

6.3.2 Struts and unit cells simulations

Strain-controlled uniaxial tensile tests were simulated using the finite-strain VEVP model with the material parameters for the micro-scale implemented in FFTMAD. To predict the mechanical behavior of the struts, a cylindrical defect-free RVE was used, a maximum strain of 0.12 was applied at maximum times of 43.25, 7.3, 0.73, and 0.073 s, which are equivalent to the strain rates 2.78×10^{-3}, 1.67×10^{-2}, 1.67×10^{-1}, and 1.67 s^{-1}, respectively, to compare the stress-strain curves with the experimental ones obtained from the 1.5 mm diameter single struts. To achieve better convergence rates and improve the results, the parameter β was scaled by 1.5.

For the BCC unit cells, strain-controlled uniaxial compression tests were simulated with FFTMAD using the finite-strain VEVP model. The parameters obtained for the microscopic and bulk parameters calibrated with the experimental data were used for the simulations. As with the single struts, the non-linear response was predicted using a defect-free RVE, and a maximum strain of 0.075 was applied at a maximum time of 4.97 s to simulate a strain rate of 1.5×10^{-3} s^{-1} to compare the results with the experimental data. In addition, to validate the implementation of the material model in FFTMAD, the same simulation, using the macroscopic parameters, same loading conditions, and material model, was performed with the commercial software *Abaqus*. To improve the convergence rate, β was multiplied by 1.5.

The mechanical behavior under tension and different strain rates of a single strut with a 1.5 mm diameter obtained experimentally and the predictions obtained with the material model using microscopic parameters are compared in Figure 6.12. The predictions with the large strain VEVP model and the calibrated parameters for the microscopic parameters agree well with the desired behavior, that is, the strain rate dependency and the dissipative VEVP response. The agreement between predictions using the fitted parameters and the experimental results validates the Bayesian inference fitting process.

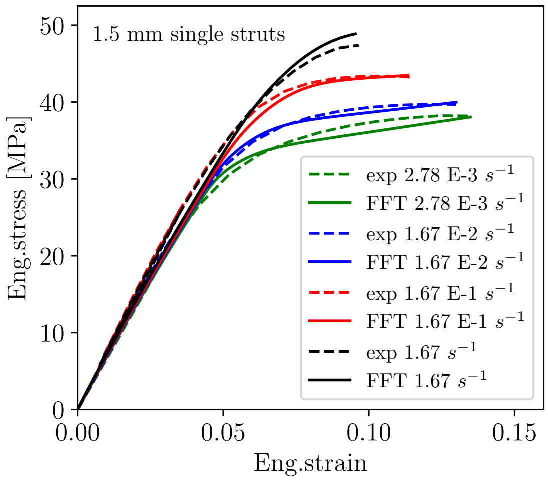

Figure 6.12: Non-linear behavior prediction using VEVP model on 1.5 mm diameter single struts using microscopic parameters.

Figure 6.13a shows the experimental and predicted behavior of the BCC unit cell with 1.5 mm diameter struts. In this case, as the material parameters for the microscopic scale were calibrated using only experimental data from tensile tests, the simulation could not predict the plastic behavior of the unit cell under compression. However, the apparent stiffness obtained for the unit cell with 1.5 mm diameter struts was 47.74 MPa, which is very close to the average experimental result, 44.1 MPa, as shown in table 5.2. This indicates that a fitting of micro parameters with only experimental data from the tensile tests of single struts is insufficient to predict material behavior under loading conditions other than uniaxial tension, as is the case with the unit cells under compression.

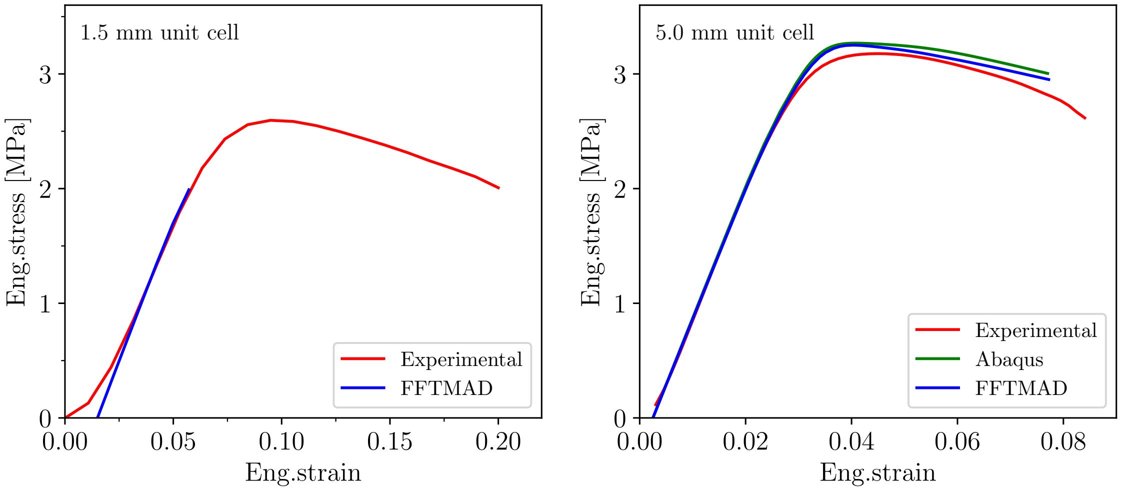

(a) **(b)**

Figure 6.13: Non-linear behavior prediction using VEVP model on (a) BCC unit cell with 1.5 mm diameter struts using microscopic parameters, and (b) BCC unit cell with 5.0 mm diameter struts using bulk parameters.

Figure 6.13b shows the stress-strain curves obtained by compression tests and simulations of a macroscopic-sized unit cell. As the parameters were fitted using all the experimental data from the bulk mechanical characterization shown in section 4.1, the stress-strain curves obtained with the macroscopic parameters, using both *Abaqus* and FFTMAD, closely align with the experimental data. Compared to the unit cell's mechanical behavior obtained using the microscopic parameters, the predictions using bulk parameters successfully replicate the expected non-linear response because there was enough experimental data to obtain the fitted parameters that predict the material's behavior under a wide range of loading conditions.

Chapter 7

Conclusions

In this work, the mechanical response of lattices fabricated by SLS in PA12 polymer has been analyzed using experimental and numerical techniques, paying special attention to the material response and the effect of the fabrication defects.

PA12 specimens printed by SLS have been characterized using a variety of experimental techniques at the macroscale using bulk specimens and at the microscale by directly studying lattices, unit cells, and single strut responses. In the bulk form, the material was tested under different loading conditions, strain rates, temperatures, and at different polymer aging times to study how the material responds to a broad set of mechanical and environmental conditions. In the case of single struts, unit cells, and lattices, experimental and numerical analysis techniques were combined. For the mechanical response, both micro-tension tests (single struts) and micro-compression tests (unit cells and lattices) were performed. For the micro and nanostructure characterization, X-ray tomography, nanoindentation, DSC, SAXS, and WAXS were used. Simulations of the different types of specimens have been performed by FEM and FFT-based homogenization. The first technique has been used for ideal full lattice experiments. On the other hand, FFT homogenization has been adapted to study microstructures obtained directly from X-ray tomography in order to quantify the effect of defects.

A summary of the conclusions achieved in this study is presented below,

- Microstructure of SLS PA12 is controlled by the size of the fabricated part, from struts to bulk specimens

  The size of the struts significantly influences the microstructure due to the limitations of the 3D printing machine's resolution, as the components are subjected to different thermal histories related to the contour and hatching strategy. First of all, since the surface roughness and pore size remain constant, smaller samples have relatively larger defects compared to their overall size. Regarding coalescence between particles, struts with diameters below 0.96 mm present a high fraction of unmelted and partially melted particles with poor particle coalescence, especially in smaller struts (0.5–0.7 mm). As the cross-section diameter increases, the consistent melting improves the quality of coalescence between particles. The different types of coalescence between particles are observed between struts and bulk material with SEM, nanoindentation maps, and optical microscopy. Furthermore, WAXS and SAXS help to quantify coalescence quality. WAXS and SAXS revealed that the γ_m phase dominates in powders and smaller struts (0.5–0.7 mm) containing partially melted particles, and γ_m evolves towards the stable $\gamma_{(001)}$ phase as the strut diameter and fraction of fully melted particles increases, peaking in the bulk material. In the case of lattices, the nanostructure resembled that of bulk material, as the time and temperature during manufacturing acted as an annealing treatment, enhancing coalescence quality.

- PA12 exhibits moderate strain rate sensitivity.

  This response is achieved both on the bulk material using standard uniaxial tests at different strain rates and at the macroscale by conventional nanoindentation and nano-impact tests on lattice nodes. Moreover, the similarity of the macro- and micro-strain rate dependency results validates the use of different testing techniques to characterize rate-dependent mechanical behavior.

- Fabrication direction has a strong effect on the mechanical response, especially in plasticity and fracture.

  At the macro-scale, PA12 presents a viscoelastic-viscoplastic behavior with moderate strain rate sensitivity on the yield stress. It behaves as an isotropic material within the elastic range, as the elastic modulus is independent of the load application direction when tested in compression. In contrast, the modulus values are slightly higher when tensile loads are applied parallel to the layers. However, the mechanical behavior of PA12 is highly anisotropic in the plastic range when tested under tension due to the much higher sensitivity to imperfections when the load is applied perpendicular to the layers. In compression, the PA12 material behaves in an isotropic manner, even in the plastic regime, as the mechanical response is much less sensitive to layer imperfections.

- Temperature and humidity strongly affect the mechanical response.

  At temperatures close to the T_g, the material is more ductile ($\geq$12 %) but suffers from a decrease in the yield stress of $\approx$ 45 % and elastic modulus of at least 30 %. On the other hand, samples aged at room temperature in a dry environment present a slight increase in stiffness by $\approx$ 1.5 % and become more fragile by at least 15 %, which is the typical behavior of a polymer that has been subjected to physical aging. Therefore, the direction of the load concerning the layer's orientation and the influence of temperature and time are essential considerations in the design of PA12 SLS-printed pieces.

- A very strong size effect on the mechanical properties, mainly stiffness and strength (*smaller is softer/weaker*), is observed between the macro and micro scales.

  Single unit cells fabricated with strut diameters in the millimetric range presented an effective elastic modulus reduction of 50 % in comparison to the macroscopic material. This reduction is monotonically related to the dimensions of the struts, leading to a size effect of the type *the smaller, the softer*. It has been found that this size effect is the combination of several factors. Porosity and surface roughness produce a reduction in the elastic modulus of $\approx$ 10 %, becoming less critical as the size increases. Therefore, this weakening effect cannot justify itself the significant loss of stiffness of unit cells. The remaining reduction is caused mainly by the partial melting of the powder, whose fraction decreases with diameter. The presence of unmelted particles is due to the contour step during the manufacturing for small diameters, as this step delivers less energy density to the process. The DSC and WAXS-SAXS analysis confirmed the presence of unmelted particles, which are less frequent as the diameter increases.

- The size effect of strut diameter is influenced by full specimen size

  In the case of macroscopic lattice specimens, the stiffness reduction with respect to macroscopic bulk samples is also present (30 % reduction) but weaker than in single cells or struts (which reached around 50 %). Moreover, the strut diameter size effect in large lattice specimens is less important. Again, the reason for this weakening is a combination of factors. On the one hand, partial melting and defects are also found in these specimens in numbers similar to those of unit cells. On the other hand, WAXS-SAXS analyses show that the nanostructure of melted areas in full lattice specimens differs from unit cells. This different nanostructure is induced by the different thermal histories that depend on the sample dimensions. In the case of large specimens, the laser passes more times through the same area, increasing the annealing degree on the samples. As a result, melted powder undergoes a phase transformation where the content of the stable γ phase and the lamellar thickness increase, enhancing the mechanical properties of the material and the quality of the bonding between particles.

- Internal pores and surface roughness control the fracture of SLS PA12 parts

  Fractures originate from crack nucleation in the defects and its propagation depends mainly on the printing direction in single struts. However, no direct correlation between failure and a crack originating in the surface or internal pores is observed. On the other hand, crack nucleation and propagation in unit cells are directly correlated with the geometry of the samples, where the crack always nucleates on the nodes that connect with a strut oriented in the load direction. Furthermore, although surface treatment does not strongly affect the mechanical properties of unit cells with diameters over 0.5 mm, nucleation of cracks in the surface of the struts is not produced.

- Numerical simulations, and FFT-based homogenization in particular, allows to quantitatively predict the effect of defects

  FFT simulations allowed us to quantify the effect of the defects in the response of the materials with respect to ideal specimens. These differences were around 10%. In addition, FFT combined with linear elastic fracture mechanics using a phase-field fracture model allows the simulation of crack propagation in the simulation of an experiment. These simulations correlate well the stress concentration areas when compared with tomographic results. However, the defect responsible for the final failure was not always identified with the combination of phase-field fracture and actual microstructure. Probably differences are due to the strong simplification of assuming an elastic-brittle response.

It also has to be remarked that other process parameters beyond specimen size and orientation influence the mechanical properties, especially when the machine is working close to its resolution limit. However, these parameters cannot be modified in commercial machines, which are optimized for macroscopic specimens. If the manufacturing strategy or printing parameters were optimized for components with microscopic dimensions, the effect of defects, poor particle coalescence, and thermal history could potentially be reduced, and the size effect might be mitigated.

Nevertheless, the use of commercial machines is mandatory in this work and in the MOAMMM project itself since it is the basis for the implementation of the results of the research in an industrial environment. In the case of standard fabrication in commercial printers, this study will help design components made up of lattice meta-materials, considering the actual behavior as a function of the cell characteristics (strut diameter) and part size. In addition, the experimental and numerical techniques, including the material model, used in this work can be used to characterize other materials, especially polymeric in both bulk and lattice form.

A general conclusion is that SLS PA12 material can be successfully used to fabricate parts composed of lattices. During the MOAMMM project, the characterization performed in this thesis has been used to design and fabricate a bicycle helmet and shoe soles with great success.

7.1 Future work

This study has addressed the mechanical behavior of PA12 samples fabricated by SLS for producing metamaterial components while making insightful contributions to understanding the root cause of the effect of sample size on the mechanical properties and the evolution of damage. However, there are areas where further research is needed. Challenges were found, especially in the additive manufacturing strategy used, which was not optimized to print samples on the micro-scale, the experimental infrastructure available to perform mechanical tests on the struts was limited, and the computational resources needed to do simulations on lattice geometries and the digital volume replicas of the tomographies were very demanding. Having identified the limitations, future studies could:

- Conduct additional tests on micro samples across a broad range of loading conditions, such as the characterization carried out on the bulk material, to obtain more experimental data for calibrating the micro parameters with BI (Bayesian inference).
- Refine the machine's printing parameters to maximize the quality and mechanical performance of printed components with dimensions close to the resolution of the printing machine, such as struts.
- Optimize the FFTMAD algorithm by combining phase-field fracture with the large strains VEVP material model to predict the samples' non-linear response and crack nucleation and propagations by using the tomographic volume replicas as RVEs and include damage. In addition, implementing an anisotropic material law could enable to understand the effect of printing direction in additive manufactured samples.

Moreover, exploring new printing strategies for SLS to build lattice structures and struts, such as the single pulse strategy proposed by Ghouse et al., 2017, could provide valuable insights that were beyond the scope of the present work. Continued investigation in these areas will be essential for designing lattice materials and could ultimately lead to the cost-effective production of components with customizable mechanical behavior for shock absorption applications in the aerospace, automotive, and medical industries, among others.

Bibliography

Al Rashid, A., Ahmed, W., Khalid, M. Y., & Koç, M. (2021). Vat photopolymerization of polymers and polymer composites: Processes and applications. *Additive Manufacturing*, *47*, 102279. https://doi.org/10.1016/j.addma.2021.102279

Ali, M., Sari, R. K., Sajjad, U., Sultan, M., & Ali, H. M. (2021). Effect of annealing on microstructures and mechanical properties of pa-12 lattice structures proceeded by multi jet fusion technology. *Additive Manufacturing*, *47*, 102285. https://doi.org/https://doi.org/10.1016/j.addma.2021.102285

Al-Othman, A., Tawalbeh, M., Temsah, O., Khan, H. A., & Hajar, A. A. (2022). Metamaterials: Classifications and characteristics. In A.-G. Olabi (Ed.), *Encyclopedia of smart materials* (pp. 46–56). Elsevier. https://doi.org/https://doi.org/10.1016/B978-0-12-815732-9.00088-7

Amani, Y., Dancette, S., Delroisse, P., Simar, A., & Maire, E. (2018). Compression behavior of lattice structures produced by selective laser melting: X-ray tomography based experimental and finite element approaches. *Acta Materialia*, *159*, 395–407. https://doi.org/https://doi.org/10.1016/j.actamat.2018.08.030

Amani, Y., Dancette, S., Luksch, J., Jung, A., & Maire, E. (2020). Micro-tensile behavior of struts extracted from an aluminum foam. *Materials Characterization*, *166*, 110456. https://doi.org/https://doi.org/10.1016/j.matchar.2020.110456

Amel, H., Moztarzadeh, H., Rongong, J., & Hopkinson, N. (2014). Investigating the behavior of laser-sintered nylon 12 parts subject to dynamic loading. *Journal of Materials Research*, *29*(17), 1852–1858. https://doi.org/10.1557/jmr.2014.150

Aranda, P., Zarzoso, G., & Segurado, J. (2022). Implementación de un esquema fft para un modelo de 'phase-field fracture': Aplicación a metales policristalinos. *Revista española de mecanica de fractura*, (3), 77–82.

Bar-Sinai, Y., Librandi, G., Bertoldi, K., & Moshe, M. (2020). Geometric charges and nonlinear elasticity of two-dimensional elastic metamaterials. *Proceedings of the National Academy of Sciences*, *117*(19), 10195–10202. https://doi.org/10.1073/pnas.1920237117

Bertoldi, K. (2017). Harnessing instabilities to design tunable architected cellular materials. *Annual Review of Materials Research*, *47*(1), 51–61. https://doi.org/10.1146/annurev-matsci-070616-123908

Briscoe, B. J., Fiori, L., & Pelillo, E. (1998). Nano-indentation of polymeric surfaces. *Journal of Physics D: Applied Physics*, *31*(19), 2395–2405. https://doi.org/10.1088/0022-3727/31/19/006

Bückmann, T., Stenger, N., Kadic, M., Kaschke, J., Frölich, A., Kennerknecht, T., Eberl, C., Thiel, M., & Wegener, M. (2012). Tailored 3d mechanical metamaterials made by dip-in direct-laser-writing optical lithography. *Advanced Materials*, *24*(20), 2710–2714. https://doi.org/10.1002/adma.201200584

Cerveny, S., Bergman, R., Schwartz, G. A., & Jacobsson, P. (2002). Dielectric α- and β-relaxations in uncured styrene butadiene rubber. *Macromolecules*, *35*(11), 4337–4342. https://doi.org/10.1021/ma010990o

Chatham, C. A., Bortner, M. J., Johnson, B. N., Long, T. E., & Williams, C. B. (2021). Predicting mechanical property plateau in laser polymer powder bed fusion additive manufacturing via the critical coalescence ratio. *Materials and Design*, *201*, 109474. https://doi.org/10.1016/j.matdes.2021.109474

Chen, P., Tang, M., Zhu, W., Yang, L., Wen, S., Yan, C., Ji, Z., Nan, H., & Shi, Y. (2018). Systematical mechanism of polyamide-12 aging and its micro-structural evolution during laser sintering. *Polymer Testing*, *67*, 370–379. https://doi.org/https://doi.org/10.1016/j.polymertesting.2018.03.035

Cheng, Y.-T., & Cheng, C.-M. (2004). Scaling, dimensional analysis, and indentation measurements. *Materials Science and Engineering: R: Reports*, *44*(4–5), 91–149. https://doi.org/10.1016/j.mser.2004.05.001

Cobian, L., Maire, E., Adrien, J., Freitas, U., Fernández-Blázquez, J., Monclús, M., & Segurado, J. (2024). Effect of sample dimensions on the stiffness of pa12 lattice materials fabricated using powder bed fusion. *Additive Manufacturing*, *93*, 104382. https://doi.org/10.1016/j.addma.2024.104382

Cobian, L., Rueda-Ruiz, M., Fernandez-Blazquez, J., Martinez, V., Galvez, F., Karayagiz, F., Lück, T., Segurado, J., & Monclus, M. (2022). Micromechanical characterization of the material response in a pa12-sls fabricated lattice structure and its correlation with bulk behavior. *Polymer Testing*, *110*, 107556. https://doi.org/https://doi.org/10.1016/j.polymertesting.2022.107556

Cook, J., Goodridge, R., & Siviour, C. (2015). Strain rate dependency of laser sintered polyamide 12. *EPJ Web of Conferences*, *94*, 02019. https://doi.org/10.1051/epjconf/20159402019

Cser, F. (2001). About the lorentz correction used in the interpretation of small angle x-ray scattering data of semicrystalline polymers. *Journal of Applied Polymer Science*, *80*(12), 2300–2308. https://doi.org/https://doi.org/10.1002/app.1335

Ćurković, P. (2021). Optimization of generatively encoded multi-material lattice structures for desired deformation behavior. *Symmetry*, *13*(2), 293. https://doi.org/10.3390/sym13020293

D. Bruson, F. C., M. Galati, & Iuliano, L. (2023). Mechanical characterisation and simulation of the tensile behaviour of polymeric additively manufactured lattice structures. *Experimental Mechanics*. https://doi.org/https://doi.org/10.1007/s11340-023-00976-5

Dadbakhsh, S., Verbelen, L., Verkinderen, O., Strobbe, D., Van Puyvelde, P., & Kruth, J.-P. (2017). Effect of pa12 powder reuse on coalescence behaviour and microstructure of sls parts. *European Polymer Journal*, *92*, 250–262. https://doi.org/10.1016/j.eurpolymj.2017.05.014

Dao, M., Chollacoop, N., Van Vliet, K., Venkatesh, T., & Suresh, S. (2001). Computational modeling of the forward and reverse problems in instrumented sharp indentation. *Acta Materialia*, *49*(19), 3899–3918. https://doi.org/10.1016/s1359-6454(01)00295-6

Deshpande, V., Fleck, N., & Ashby, M. (2001). Effective properties of the octet-truss lattice material. *Journal of the Mechanics and Physics of Solids*, *49*(8), 1747–1769. https://doi.org/10.1016/s0022-5096(01)00010-2

Domininghaus, H. (1993). *Plastics for engineers: Material, properties, applications*. Hanser.

Drzeżdżon, J., Jacewicz, D., Sielicka, A., & Chmurzyński, L. (2019). Characterization of polymers based on differential scanning calorimetry based techniques. *TrAC Trends in Analytical Chemistry*, *110*, 51–56. https://doi.org/10.1016/j.trac.2018.10.037

Ebnesajjad, S., & Khaladkar, P. R. (2005). 10 - failure analysis. In S. Ebnesajjad & P. R. Khaladkar (Eds.), *Fluoropolymers applications in the chemical processing industries* (pp. 315–357). William Andrew Publishing. https://doi.org/https://doi.org/10.1016/B978-081551502-9.50013-2

EOSGmbH. (2024). *Pa 2200 - polyamide 12* [Last accessed: 2024-10-14]. https://store.eos.info/products/pa-2200-polyamide-12

EPO. (2023). Innovation trends in additive manufacturing. patents in 3d printing technologies. *European Patent Office*, [Last accessed: 2024-03–25]. https://doi.org/https://www.oepm.es/export/sites/portal/comun/documentos_relacionados/Noticias/2023/2023_09_19_Nuevo_Informe_EPO_AM_Study_190923.pdf

Feng, J., Liu, B., Lin, Z., & Fu, J. (2021). Isotropic octet-truss lattice structure design and anisotropy control strategies for implant application. *Materials & Design*, *203*, 109595. https://doi.org/https://doi.org/10.1016/j.matdes.2021.109595

Ferreira, I., Melo, C., Neto, R., Machado, M., Alves, J., & Mould, S. (2020). Study of the annealing influence on the mechanical performance of pa12 and pa12 fibre reinforced fff printed specimens. *Rapid Prototyping Journal*, *26*(10), 1761–1770. https://doi.org/https://doi.org/10.1108/RPJ-10-2019-0278

Findeisen, C., Hohe, J., Kadic, M., & Gumbsch, P. (2017). Characteristics of mechanical metamaterials based on buckling elements. *Journal of the Mechanics and Physics of Solids*, *102*, 151–164. https://doi.org/10.1016/j.jmps.2017.02.011

Flodberg, G., Pettersson, H., & Yang, L. (2018). Pore analysis and mechanical performance of selective laser sintered objects. *Additive Manufacturing*, *24*, 307–315. https://doi.org/https://doi.org/10.1016/j.addma.2018.10.001

Flores, I., Kretzschmar, N., Azman, A. H., Chekurov, S., Pedersen, D. B., & Chaudhuri, A. (2020). Implications of lattice structures on economics and productivity of metal powder bed fusion. *Additive Manufacturing*, *31*, 100947. https://doi.org/10.1016/j.addma.2019.100947

Geng, X., Ma, L., Liu, C., Zhao, C., & Yue, Z. (2018). A fem study on mechanical behavior of cellular lattice materials based on combined elements. *Materials Science and Engineering: A*, *712*, 188–198. https://doi.org/https://doi.org/10.1016/j.msea.2017.11.082

Ghouse, S., Babu, S., Van Arkel, R. J., Nai, K., Hooper, P. A., & Jeffers, J. R. (2017). The influence of laser parameters and scanning strategies on the mechanical properties of a stochastic porous material. *Materials & amp; Design*, *131*, 498–508. https://doi.org/10.1016/j.matdes.2017.06.041

Gibson, I., Rosen, D. W., Stucker, B., & Khorasani, M. (2021). *Additive manufacturing technologies*. Springer International Publishing.

Gill, P., Moghadam, T. T., & Ranjbar, B. (2010). Differential scanning calorimetry techniques: Applications in biology and nanoscience. *Journal of biomolecular techniques*, *21 4*, 167–193.

GrandViewResearch. (2016). *Metamaterial market size, share & trends analysis report by product (electromagnetic, terahertz, photonic, tunable, frequency selective surface, non-linear), by application, end-use, and segment forecasts, 2018 - 2025* [Accessed: 2024-03-11]. https://www.grandviewresearch.com/industry-analysis/metamaterials-market

Greco, R., & Nicolais, L. (1976). Glass transition temperature in nylons. *Polymer*, *17*(12), 1049–1053. https://doi.org/10.1016/0032-3861(76)90005-7

Güemes Gordo, A., & Martín Piris, N. (2012). *Ciencia de materiales para ingenieros*. Pearson Educación.

Guo, C., & Luo, Y. (2023). Light people: Prof. sir john pendry, father of metamaterials, spoke about the future of meta. *Light: Science & Applications*, *12*(1). https://doi.org/10.1038/s41377-023-01082-w

Haghpanah, B., Oftadeh, R., Papadopoulos, J., & Vaziri, A. (2013). Self-similar hierarchical honeycombs. *Proceedings of the Royal Society A: Mathematical, Physical and Engineering Sciences*, *469*(2156), 20130022. https://doi.org/10.1098/rspa.2013.0022

Hardiman, M., Vaughan, T., & McCarthy, C. (2017). A review of key developments and pertinent issues in nanoindentation testing of fibre reinforced plastic microstructures. *Composite Structures*, *180*, 782–798. https://doi.org/https://doi.org/10.1016/j.compstruct.2017.08.004

Hejmady, P., van Breemen, L. C., Hermida-Merino, D., Anderson, P. D., & Cardinaels, R. (2022). Laser sintering of pa12 particles studied by in-situ optical, thermal and x-ray characterization. *Additive Manufacturing*, *52*, 102624. https://doi.org/https://doi.org/10.1016/j.addma.2022.102624

Herman, G. (2010). *Fundamentals of computerized tomography*. https://doi.org/10.1007/978-1-84628-723-7

Hossain, U., Ghouse, S., Nai, K., & Jeffers, J. R. (2021). Mechanical and morphological properties of additively manufactured ss316l and ti6al4v micro-struts as a function of build angle. *Additive Manufacturing*, *46*, 102050. https://doi.org/https://doi.org/10.1016/j.addma.2021.102050

Huang, Z., Chen, Z., Zhu, L., Xie, G., Hua, Y., Zhao, D., & Hu, N. (2023). Implementation of parametric modeling to design miura origami-inspired canopy toward adaptive urban habitat. *Architecture, Structures and Construction*, *4*(1), 113–122. https://doi.org/10.1007/s44150-023-00100-0

Hutchinson, J. M. (1995). Physical aging of polymers. *Progress in Polymer Science*, *20*(4), 703–760. https://doi.org/https://doi.org/10.1016/0079-6700(94)00001-I

Jiao, P., Mueller, J., Raney, J. R., Zheng, X., & Alavi, A. H. (2023). Mechanical metamaterials and beyond. *Nature Communications*, *14*(1). https://doi.org/10.1038/s41467-023-41679-8

José Baruchel, E. M., Jean-Yves Buffiere. (2000). *X-ray tomography in material science*. Hermes Science.

Kimberley, J., Lamberson, L., & Mates, S. (2019). *Dynamic behavior of materials, volume 1*. Springer International Publishing. https://doi.org/https://doi.org/10.1007/978-3-319-95089-1

Kohli, N., Theodoridis, K., Hall, T. A., Sanz-Pena, I., Gaboriau, D. C., & van Arkel, R. J. (2023). Bioreactor analyses of tissue ingrowth, ongrowth and remodelling around implants: An alternative to live animal testing. *Frontiers in Bioengineering and Biotechnology*, *11*. https://doi.org/10.3389/fbioe.2023.1054391

Kwiatkowska, M., Pelech, R., Jedrzejewska, A., Moszynski, D., & Pelech, I. (2020). Different approaches to oxygen functionalization of multi-walled carbon nanotubes and their effect on mechanical and thermal properties of polyamide 12 based composites. *Polymers*, *12*(2), 308. https://doi.org/10.3390/polym12020308

Lammens, N., Kersemans, M., De Baere, I., & Van Paepegem, W. (2017). On the visco-elasto-plastic response of additively manufactured polyamide-12 (pa-12) through selective laser sintering. *Polymer Testing*, *57*, 149–155. https://doi.org/https://doi.org/10.1016/j.polymertesting.2016.11.032

Lhuissier, P., de Formanoir, C., Martin, G., Dendievel, R., & Godet, S. (2016). Geometrical control of lattice structures produced by ebm through chemical etching: Investigations at the scale of individual struts. *Materials and Design*, *110*, 485–493. https://doi.org/https://doi.org/10.1016/j.matdes.2016.08.029

Li, C., Snarr, S. E., Denlinger, E. R., Irwin, J. E., Gouge, M. F., Michaleris, P., & Beaman, J. J. (2021). Experimental parameter identification for part-scale thermal modeling of selective laser sintering of pa12. *Additive Manufacturing*, *48*, 102362. https://doi.org/https://doi.org/10.1016/j.addma.2021.102362

Liu, F., Terakawa, T., Long, S., & Komori, M. (2024). Rigid-foldable cylindrical origami with tunable mechanical behaviors. *Scientific Reports*, *14*(1). https://doi.org/10.1038/s41598-023-50353-4

Liu, L., Boldon, L., Urquhart, M., & Wang, X. (2013). Small and wide angle x-ray scattering studies of biological macromolecules in solution. *Journal of Visualized Experiments*, (71). https://doi.org/10.3791/4160

Liu, X., Tey, W. S., Choo, J. Y. C., Chen, J., Tan, P., Cai, C., Ong, A., Zhao, L., & Zhou, K. (2021). Enhancing the mechanical strength of multi jet fusion–printed polyamide 12 and its glass fiber-reinforced composite via high-temperature annealing. *Additive Manufacturing*, *46*, 102205. https://doi.org/https://doi.org/10.1016/j.addma.2021.102205

Lucarini, S., Cobian, L., Voitus, A., & Segurado, J. (2022). Adaptation and validation of fft methods for homogenization of lattice based materials. *Computer Methods in Applied Mechanics and Engineering*, *388*, 114223. https://doi.org/https://doi.org/10.1016/j.cma.2021.114223

Lucarini, S., & Segurado, J. (2019). An algorithm for stress and mixed control in galerkin-based fft homogenization. *International Journal for Numerical Methods in Engineering*, *119*(8), 797–805.

Lucarini, S., Upadhyay, M. V., & Segurado, J. (2021). Fft based approaches in micromechanics: Fundamentals, methods and applications. *Modelling and Simulation in Materials Science and Engineering*, *30*(2), 023002. https://doi.org/10.1088/1361-651x/ac34e1

Lucarini, S., Cobian, L., Voitus, A., & Segurado, J. (2021). Adaptation and validation of fft methods for homogenization of lattice based materials. *Computer Methods in Applied Mechanics and Engineering*.

Lupone, F., Padovano, E., Casamento, F., & Badini, C. (2021). Process phenomena and material properties in selective laser sintering of polymers: A review. *Materials (Basel)*, *15*, 183. https://doi.org/https://doi.org/10.3390/ma15010183

Lv, C., Krishnaraju, D., Konjevod, G., Yu, H., & Jiang, H. (2014). Origami based mechanical metamaterials. *Scientific Reports*, *4*(1). https://doi.org/10.1038/srep05979

Ma, N., Liu, W., Ma, L., He, S., Liu, H., Zhang, Z., Sun, A., Huang, M., & Zhu, C. (2020). Crystal transition and thermal behavior of nylon 12. *e-Polymers*, *20*(1), 346–352. https://doi.org/doi:10.1515/epoly-2020-0039

Maconachie, T., Leary, M., Lozanovski, B., Zhang, X., Qian, M., Faruque, O., & Brandt, M. (2019). Slm lattice structures: Properties, performance, applications and challenges. *Materials & Design*, *183*, 108137. https://doi.org/10.1016/j.matdes.2019.108137

Manaia, J. P., Pires, F. A., de Jesus, A. M., & Wu, S. (2020). Mechanical response of three semi crystalline polymers under different stress states: Experimental investigation and modelling. *Polymer Testing*, *81*, 106156. https://doi.org/10.1016/j.polymertesting.2019.106156

Medeiros, L. G., Da Costa Mattos, H., & Reis, J. (2016). Elasto-viscoplastic behaviour of a polyamide under cyclic tension.

Melro, A., Camanho, P., Andrade Pires, F., & Pinho, S. (2013). Micromechanical analysis of polymer composites reinforced by unidirectional fibres: Part i – constitutive modelling. *International Journal of Solids and Structures*, *50*(11–12), 1897–1905. https://doi.org/10.1016/j.ijsolstr.2013.02.009

Miehe, C., Welschinger, F., & Hofacker, M. (2010). Thermodynamically consistent phase-field models of fracture: Variational principles and multi-field fe implementations. *International Journal for Numerical Methods in Engineering*, *83*(10), 1273–1311. https://doi.org/10.1002/nme.2861

Mir, M., Ali, M. N., Sami, J., & Ansari, U. (2014). Review of mechanics and applications of auxetic structures. *Advances in Materials Science and Engineering*, *2014*, 1–17. https://doi.org/10.1155/2014/753496

MOAMMM. (2024). *Public repository from the european project moammm* [Accessed: 2024-09-09]. https://gitlab.uliege.be/moammm

Monclus, M., & Jennett, N. (2011). In search of validated measurements of the properties of viscoelastic materials by indentation with sharp indenters. *Philosophical Magazine*, *91*(7-9), 1308–1328. https://doi.org/10.1080/14786435.2010.504197

Moran, B., Ortiz, M., & Shih, C. F. (1990). Formulation of implicit finite element methods for multiplicative finite deformation plasticity. *International Journal for Numerical Methods in Engineering*, *29*(3), 483–514. https://doi.org/10.1002/nme.1620290304

Morelle, X., Bahrami, A., Lani, F., Melchior, M., Nysten, B., Bailly, C., & Pardoen, T. (2014). Characterization and modeling of the time-dependent behavior of the rtm6 structural epoxy involving recovery, creep and back stress.

Mousanezhad, D., Haghpanah, B., Ghosh, R., Hamouda, A. M., Nayeb-Hashemi, H., & Vaziri, A. (2016). Elastic properties of chiral, anti-chiral, and hierarchical honeycombs: A simple energy-based approach. *Theoretical and Applied Mechanics Letters*, *6*(2), 81–96. https://doi.org/10.1016/j.taml.2016.02.004

Nguyen, V.-D., Lani, F., Pardoen, T., Morelle, X., & Noels, L. (2016). A large strain hyperelastic viscoelastic-viscoplastic-damage constitutive model based on a multi-mechanism non-local damage continuum for amorphous glassy polymers. *International Journal of Solids and Structures*, *96*, 192–216. https://doi.org/10.1016/j.ijsolstr.2016.06.008

Nishida, M., Natsume, R., & Hayashi, M. (2013). Strain rate dependence of yield condition of polyamide 11. *Conference Proceedings of the Society for Experimental Mechanics Series*, 121–127. https://doi.org/10.1007/978-3-319-00771-7_15

NovaOne. (2023). *Additive manufacturing market size, share & trends analysis report by component, by printer type, by technology, by software, by application, by vertical, by material, by region- global industry analysis, share, growth, regional outlook and forecasts, 2023-2032* [Last accessed: 2024-03-21]. https://www.novaoneadvisor.com/report/additive-manufacturing-market

Oliver, W., & Pharr, G. (1992). An improved technique for determining hardness and elastic modulus using load and displacement sensing indentation experiments. *Journal of Materials Research*, *7*(6), 1564–1583. https://doi.org/10.1557/jmr.1992.1564

Paolucci, F., Peters, G. W. M., & Govaert, L. E. (2020). Plasticity-controlled failure of sintered and molded polyamide 12: Influence of temperature and water absorption. *Journal of Applied Polymer Science*, *137*(14), 48525. https://doi.org/https://doi.org/10.1002/app.48525

Parthasarathy, J., Starly, B., & Raman, S. (2011). A design for the additive manufacture of functionally graded porous structures with tailored mechanical properties for biomedical applications. *Journal of Manufacturing Processes*, *13*(2), 160–170. https://doi.org/10.1016/j.jmapro.2011.01.004

Pendry, J., Holden, A., Robbins, D., & Stewart, W. (1999). Magnetism from conductors and enhanced nonlinear phenomena. *IEEE Transactions on Microwave Theory and Techniques*, *47*(11), 2075–2084. https://doi.org/10.1109/22.798002

Picard, M., Mohanty, A. K., & Misra, M. (2020). Recent advances in additive manufacturing of engineering thermoplastics: Challenges and opportunities. *RSC Advances*, *10*(59), 36058–36089. https://doi.org/10.1039/d0ra04857g

PrecedenceResearch. (2022). *Metamaterials market (by product: Electromagnetic, terahertz, tunable, photonic, frequency selective surface; by application: Antenna and radar, sensors, cloaking devices, super lens, light, sound filtering; by end use: Healthcare, telecommunication, aerospace and defense, electronics, automotive) - global industry analysis, size, share, growth, trends, regional outlook, and forecast 2023-2032* [Accessed: 2024-02-20]. https://www.precedenceresearch.com/metamaterials-market

Pukánszky Jr., B., Bagdi, K., Tóvölgyi, Z., Varga, J., Botz, L., Hudak, S., Dóczi, T., & Pukánszky, B. (2008). Effect of interactions, molecular and phase structure on the properties of polyurethane elastomers. *Colloids for Nano- and Biotechnology*, 218–224. https://doi.org/10.1007/2882_2008_102

Rafsanjani, A., & Pasini, D. (2016). Bistable auxetic mechanical metamaterials inspired by ancient geometric motifs. *Extreme Mechanics Letters*, *9*, 291–296. https://doi.org/10.1016/j.eml.2016.09.001

Rigaku. (2024). *Industrial saxs/waxs. rigaku holdings corporation* [Accessed: 2024-09-02]. https://rigaku.com/resources/techniques/industrial-saxs-waxs

Rueda-Ruiz, M. (2021). *Experimental and computational micromechanics of fibre-reinforced polymer composites at high strainrates* [Doctoral dissertation, Universidad Politécnica de Madrid]. https://doi.org/https://doi.org/10.20868/UPM.thesis.67638

Rueda-Ruiz, M., Beake, B. D., & Molina-Aldareguia, J. M. (2020). New instrumentation and analysis methodology for nano-impact testing. *Materials & Design*, *192*, 108715. https://doi.org/10.1016/j.matdes.2020.108715

S. Gogolewski, K. C., & Gastorek, M. (1980). Effect of annealing on thermal properties and crystalline structure of polyamides. nylon 12 (polylaurolactam). *Colloid and Polymer Science*, *258*, 1130–1136. https://doi.org/https://doi.org/10.1007/BF01382456

Saadatkhah, N., Carillo Garcia, A., Ackermann, S., Leclerc, P., Latifi, M., Samih, S., Patience, G. S., & Chaouki, J. (2019). Experimental methods in chemical engineering: Thermogravimetric analysis—tga. *The Canadian Journal of Chemical Engineering*, *98*(1), 34–43. https://doi.org/10.1002/cjce.23673

Salmoria, G., Leite, J., Vieira, L., Pires, A., & Roesler, C. (2012). Mechanical properties of pa6/pa12 blend specimens prepared by selective laser sintering. *Polymer Testing*, *31*(3), 411–416. https://doi.org/https://doi.org/10.1016/j.polymertesting.2011.12.006

Schob, D., Sagradov, I., Roszak, R., Sparr, H., Franke, R., Ziegenhorn, M., Kupsch, A., Leonard, F., Müller, B., & Bruno, G. (2020). Experimental determination and numerical simulation of material and damage behaviour of 3d printed polyamide 12 under cyclic loading. *Engineering Fracture Mechanics*, *229*, 106841. https://doi.org/10.1016/j.engfracmech.2019.106841

ScienceDirect. (2024). *Elsevier: Sciencedirect search platform* [Last accessed: 2024-03-14]. https://www.sciencedirect.com

Scott, C. (2023). *Wohlers report 2023 unveils continued double-digit growth* [Last accessed: 2024-03-21]. https://wohlersassociates.com/news/wohlers-report-2023-unveils-continued-double-digit-growth/

Segurado, J., & Llorca, J. (2013). Simulation of the deformation of polycrystalline nanostructured ti by computational homogenization [Selected Publications of the EU FP7 project VIRTUAL NANOTITANIUM (VINAT)"Theoretical analysis and virtual testing of titanium-based nanomaterials”]. *Computational Materials Science*, *76*, 3–11. https://doi.org/https://doi.org/10.1016/j.commatsci.2013.03.008

Seltzer, R., de la Escalera, F. M., & Segurado, J. (2011). Effect of water conditioning on the fracture behavior of pa12 composites processed by selective laser sintering. *Materials Science and Engineering: A*, *528*(22), 6927–6933. https://doi.org/https://doi.org/10.1016/j.msea.2011.05.045

Serrano-Munoz, I., Buffiere, J.-Y., Mokso, R., Verdu, C., & Nadot, Y. (2017). Location, location & size: Defects close to surfaces dominate fatigue crack initiation. *Scientific Reports*, *7*(1). https://doi.org/10.1038/srep45239

Shaikeea, A., Hahn, D., Gandhi, V., Cui, H., Zheng, X., & Deshpande, V. (2024). The anomalous crack growth behaviour of an elastic-brittle octet-truss architected solid. *Journal of the Mechanics and Physics of Solids*, *190*, 105728. https://doi.org/https://doi.org/10.1016/j.jmps.2024.105728

Sim, Y. H., Yun, M. J., Lee, D. Y., & Cha, S. I. (2021). Origami-foldable tessellated crystalline-si solar cell module with metal textile-based stretchable connections. *Solar Energy Materials and Solar Cells*, *231*, 111318. https://doi.org/10.1016/j.solmat.2021.111318

Siviour, C., & Jordan, J. (2016). High strain rate mechanics of polymers: A review. *Journal of Dynamic Behavior of Materials*, *2*. https://doi.org/10.1007/s40870-016-0052-8

Smith, D. R., Padilla, W. J., Vier, D. C., Nemat-Nasser, S. C., & Schultz, S. (2000). Composite medium with simultaneously negative permeability and permittivity. *Phys. Rev. Lett.*, *84*, 4184–4187. https://doi.org/10.1103/PhysRevLett.84.4184

Smith, L., Hayes, B., Ford, K., Smith, E., Flores, D., & MacCurdy, R. (2024). Tunable metamaterials for impact mitigation. *Advanced Materials Technologies*. https://doi.org/10.1002/admt.202301668

Sombatmai, A., Uthaisangsuk, V., Wongwises, S., & Promoppatum, P. (2021). Multiscale investigation of the influence of geometrical imperfections, porosity, and size-dependent features on mechanical behavior of additively manufactured ti-6al-4v lattice struts. *Materials & Design*, *209*, 109985. https://doi.org/https://doi.org/10.1016/j.matdes.2021.109985

Suard, M., Martin, G., Lhuissier, P., Dendievel, R., Vignat, F., Blandin, J., & Villeneuve, F. (2015). Mechanical equivalent diameter of single struts for the stiffness prediction of lattice structures produced by electron beam melting. *Additive Manufacturing*, *8*, 124–131. https://doi.org/10.1016/j.addma.2015.10.002

Sun, Q., Rizvi, G., Bellehumeur, C., & Gu, P. (2008). Effect of processing conditions on the bonding quality of fdm polymer filaments. *Rapid Prototyping Journal*, *14*(2), 72–80. https://doi.org/10.1108/13552540810862028

Tancogne-Dejean, T., Spierings, A. B., & Mohr, D. (2016). Additively-manufactured metallic micro-lattice materials for high specific energy absorption under static and dynamic loading. *Acta Materialia*, *116*, 14–28. https://doi.org/10.1016/j.actamat.2016.05.054

Tofail, S. A., Koumoulos, E. P., Bandyopadhyay, A., Bose, S., O'Donoghue, L., & Charitidis, C. (2018). Additive manufacturing: Scientific and technological challenges, market uptake and opportunities. *Materials Today*, *21*(1), 22–37. https://doi.org/10.1016/j.mattod.2017.07.001

Touris, A., Turcios, A., Mintz, E., Pulugurtha, S. R., Thor, P., Jolly, M., & Jalgaonkar, U. (2020). Effect of molecular weight and hydration on the tensile properties of polyamide 12. *Results in Materials*, *8*, 100149. https://doi.org/https://doi.org/10.1016/j.rinma.2020.100149

Vanderesse, N., Maire, É., Chabod, A., & Buffière, J.-Y. (2011). Microtomographic study and finite element analysis of the porosity harmfulness in a cast aluminium alloy. *International Journal of Fatigue*, *33*(12), 1514–1525. https://doi.org/https://doi.org/10.1016/j.ijfatigue.2011.06.010

Veselago, V. G. (1968). The electrodynamics of substances with simultaneously negative values of ϵ and μ. *Soviet Physics Uspekhi*, *10*(4), 509–514.

Vondrejc, J., Zeman, J., & Marek, I. (2014). An fft-based galerkin method for homogenization of periodic media. *Comput. Math. Appl.*, *68*, 156–173.

Wang, P., Yang, F., Zheng, B., Li, P., Wang, R., Li, Y., Fan, H., & Li, X. (2023). Breaking the tradeoffs between different mechanical properties in bioinspired hierarchical lattice metamaterials. *Advanced Functional Materials*, *33*(45). https://doi.org/10.1002/adfm.202305978

Wheeler, J. M. (2009). *Nanoindentation under dynamic conditions* [Doctoral dissertation, Apollo - University of Cambridge Repository]. https://doi.org/10.17863/CAM.14247

Willot, F. (2014). Fourier-based schemes for computing the mechanical response of composites with accurate local fields. *Comptes Rendus Mécanique*, *343*. https://doi.org/10.1016/j.crme.2014.12.005

Wu, L., Anglade, C., Cobian, L., Monclus, M., Segurado, J., Karayagiz, F., Freitas, U., & Noels, L. (2023). Bayesian inference of high-dimensional finite-strain visco-elastic–visco-plastic model parameters for additive manufactured polymers and neural network based material parameters generator. *International Journal of Solids and Structures*, *283*, 112470. https://doi.org/10.1016/j.ijsolstr.2023.112470

Wu, M., Linne, M., Forien, J.-B., Barton, N. R., Ye, J., Hazeli, K., Perron, A., Bertsch, K., Wang, Y. M., & Voisin, T. (2024). Additively manufactured β-ti5553 with laser powder bed fusion: Microstructures and mechanical properties of bulk and lattice parts. *Journal of Materials Processing Technology*, 118354. https://doi.org/https://doi.org/10.1016/j.jmatprotec.2024.118354

Wu, W., Hu, W., Qian, G., Liao, H., Xu, X., & Berto, F. (2019). Mechanical design and multifunctional applications of chiral mechanical metamaterials: A review. *Materials & Design*, *180*, 107950. https://doi.org/10.1016/j.matdes.2019.107950

Wu, W., Qi, D., Liao, H., Qian, G., Geng, L., Niu, Y., & Liang, J. (2018). Deformation mechanism of innovative 3d chiral metamaterials. *Scientific Reports*, *8*(1). https://doi.org/10.1038/s41598-018-30737-7

Wudy, K., & Drummer, D. (2019). Aging effects of polyamide 12 in selective laser sintering: Molecular weight distribution and thermal properties. *Additive Manufacturing*, *25*, 1–9. https://doi.org/https://doi.org/10.1016/j.addma.2018.11.007

Yang, D., Jin, L., Martinez, R. V., Bertoldi, K., Whitesides, G. M., & Suo, Z. (2016). Phase-transforming and switchable metamaterials. *Extreme Mechanics Letters*, *6*, 1–9. https://doi.org/10.1016/j.eml.2015.11.004

Youssef, S., Maire, E., & Gaertner, R. (2005). Finite element modelling of the actual structure of cellular materials determined by x-ray tomography. *Acta materialia*, *53*(3), 719–730.

Yu, X., Zhou, J., Liang, H., Jiang, Z., & Wu, L. (2018). Mechanical metamaterials associated with stiffness, rigidity and compressibility: A brief review. *Progress in Materials Science*, *94*, 114–173. https://doi.org/https://doi.org/10.1016/j.pmatsci.2017.12.003

Zarringhalam, H., Hopkinson, N., Kamperman, N., & de Vlieger, J. (2006). Effects of processing on microstructure and properties of sls nylon 12. *Materials Science and Engineering*, *435–436*, 172–180. https://doi.org/10.1016/j.msea.2006.07.084

Zarzoso, G. FFT implementation of a microscopic chemo-mechanical model for damage in lithium batteries. *First Year Assessment at IMDEA Materials*. 2023.

Zheng, X., Lee, H., Weisgraber, T. H., Shusteff, M., DeOtte, J., Duoss, E. B., Kuntz, J. D., Biener, M. M., Ge, Q., Jackson, J. A., & et al. (2014). Ultralight, ultrastiff mechanical metamaterials. *Science*, *344*(6190), 1373–1377. https://doi.org/10.1126/science.1252291

Zhu, Z., & Majewski, C. (2020). Understanding pore formation and the effect on mechanical properties of high speed sintered polyamide-12 parts: A focus on energy input. *Materials & Design*, *194*, 108937. https://doi.org/https://doi.org/10.1016/j.matdes.2020.108937

Annex 1

Material properties of EOS PA2200

Table 1: EOS PA2200 highlighted properties from the material data sheet available at EOSGmbH, 2024 webpage.

Material Property	Value
Tensile Modulus X/Y/Z	1700/1700/1700 MPa
Tensile Strenght X/Y/Z	50/50/50 MPa
Strain at break X/Y/Z	20/20/10 %
Melting temperature	176 ℃

EOS PA2200 powder particle size

An analysis of the particle size distribution was carried out on new virgin powder, old powder, the powder left after the printing process, and a 50/50 mix of both powders, the mix used for printing. The overall average powder size is around 55 µm. The average particle size of each powder type is shown in table 2. The analysis data is shown in Figure 1.

Figure 2 shows SEM images of the new and old powders. The particles appear irregular, with rounded and slightly elongated forms and a homogenous size distribution. There are no major differences between the morphology and sizes of new and old powders.

Table 2: Average particle size of EOS PA2200 new, mix and old powder. D50 means that 50 % of particles are smaller and larger than the specific value.

Powder	D50 diameter (mm)
New	57.66
Mixed	55.64
Old	54.42

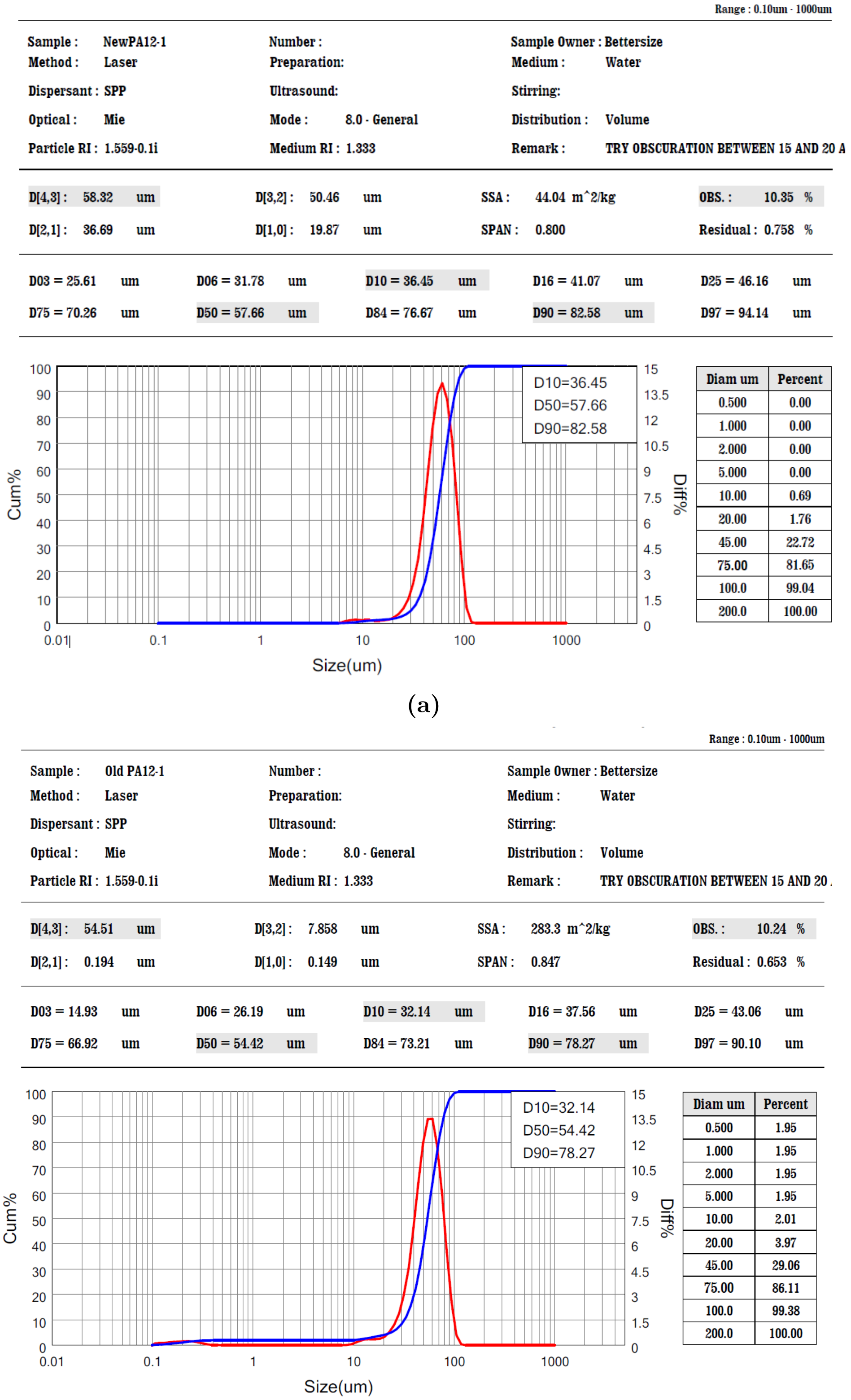

Range : 0.10um - 1000um

Sample : NewPA12-1
Method : Laser
Dispersant : SPP
Optical : Mie
Particle RI : 1.559-0.1i
Number :
Preparation:
Ultrasound:
Mode : 8.0 - General
Medium RI : 1.333
Sample Owner : Bettersize
Medium : Water
Stirring:
Distribution : Volume
Remark : TRY OBSCURATION BETWEEN 15 AND 20 A

D[4,3] : 58.32 um
D[3,2] : 50.46 um
SSA : 44.04 m^2/kg
OBS. : 10.35 %
D[2,1] : 36.69 um
D[1,0] : 19.87 um
SPAN : 0.800
Residual : 0.758 %

D03 = 25.61 um
D06 = 31.78 um
D10 = 36.45 um
D16 = 41.07 um
D25 = 46.16 um
D75 = 70.26 um
D50 = 57.66 um
D84 = 76.67 um
D90 = 82.58 um
D97 = 94.14 um

Diam um	Percent
0.500	0.00
1.000	0.00
2.000	0.00
5.000	0.00
10.00	0.69
20.00	1.76
45.00	22.72
75.00	81.65
100.0	99.04
200.0	100.00

(a)

Range : 0.10um - 1000um

Sample : Old PA12-1
Method : Laser
Dispersant : SPP
Optical : Mie
Particle RI : 1.559-0.1i
Number :
Preparation:
Ultrasound:
Mode : 8.0 - General
Medium RI : 1.333
Sample Owner : Bettersize
Medium : Water
Stirring:
Distribution : Volume
Remark : TRY OBSCURATION BETWEEN 15 AND 20 .

D[4,3] : 54.51 um
D[3,2] : 7.858 um
SSA : 283.3 m^2/kg
OBS. : 10.24 %
D[2,1] : 0.194 um
D[1,0] : 0.149 um
SPAN : 0.847
Residual : 0.653 %

D03 = 14.93 um
D06 = 26.19 um
D10 = 32.14 um
D16 = 37.56 um
D25 = 43.06 um
D75 = 66.92 um
D50 = 54.42 um
D84 = 73.21 um
D90 = 78.27 um
D97 = 90.10 um

Diam um	Percent
0.500	1.95
1.000	1.95
2.000	1.95
5.000	1.95
10.00	2.01
20.00	3.97
45.00	29.06
75.00	86.11
100.0	99.38
200.0	100.00

(b)

Figure 1: Particle size distribution analysis data of (a) new and (b) old powders.

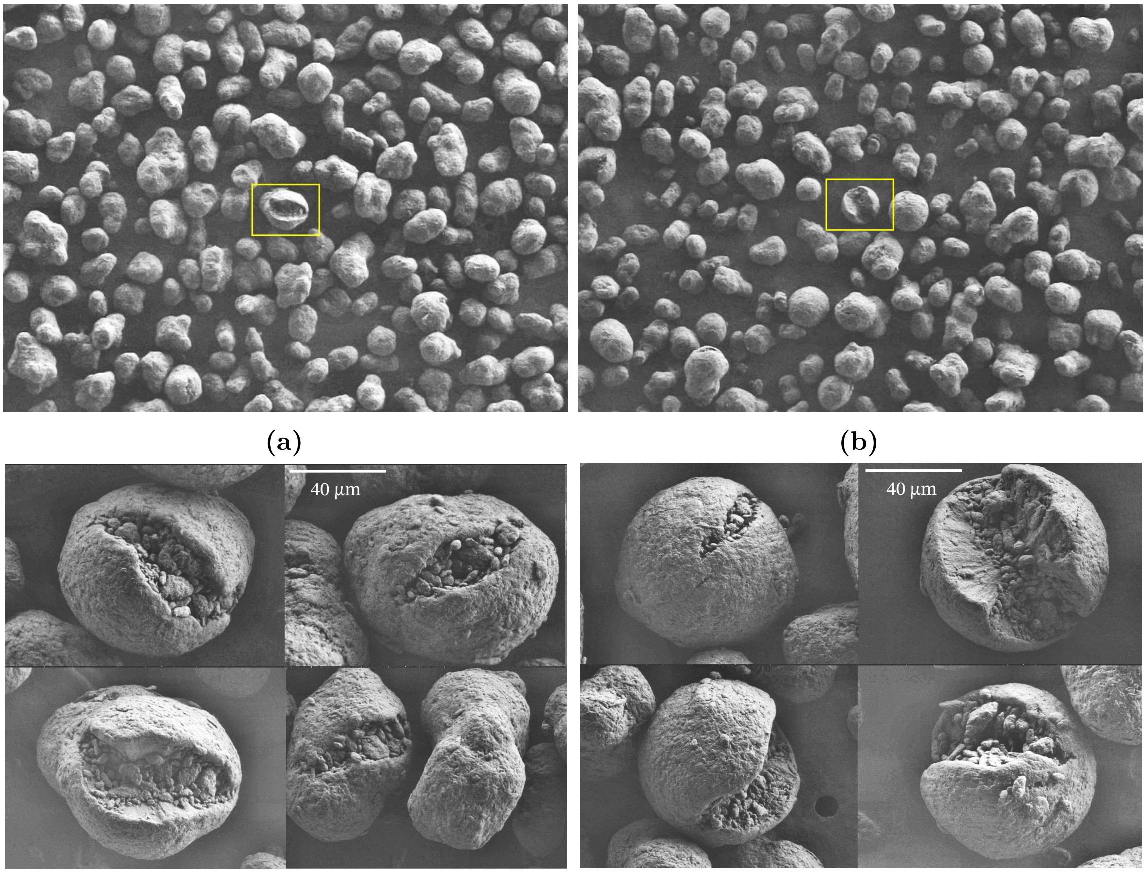

(a) (b)

(c) (d)

Figure 2: SEM images of (a) new and (b) old powders, and magnified images of (c) new and (d) old particle powders.

Annex 2

Tensile properties of PA12 aged for 22 months

Table 3: Average tensile properties with a standard deviation of aged PA12 after 22 months.

Batch / time	**2 / 22 mo**				
$\dot{\varepsilon}$ $[s^{-1}]$	**Lyr. Dir.**	**E [GPa]**	σ_y **[MPa]**	**UTS [MPa]**	**A%**
$\mathbf{7.37 \times 10^{-4}}$	**H**	1.66 ± 0.03	25.4 ± 0.4	41 ± 3	6 ± 2
	V	1.629 ± 0.009	25 ± 1	43.6 ± 0.7	13.0 ± 0.8
$\mathbf{7.37 \times 10^{-3}}$	**H**	1.70 ± 0.06	30.8 ± 0.9	46 ± 1	8 ± 2
	V	1.54 ± 0.02	26 ± 1	43.8 ± 0.4	13 ± 3
$\mathbf{7.37 \times 10^{-2}}$	**H**	1.788 ± 0.006	34.6 ± 0.3	48.5 ± 0.5	6.4 ± 0.8
	V	1.67 ± 0.01	30 ± 2	48.3 ± 0.5	11 ± 1

Annex 3

WAXS patterns of tested samples

The next figures show the WAXS patterns of all the samples tested. The figures are arranged in a sequence showing the intensity evolution of γ and γ_m peaks as the sample size increases. Figure 3 shows the pattern of the powders, where γ_m peak intensity is higher than γ. Figure 5 present the struts with 0.5 mm diameters, whose patterns are the most similar to the powders, and the intensity of γ and γ_m peaks are almost the same, being γ_m slightly higher in Figure 5a. Struts with oblique layers and 0.5 mm diameters present the lowest printing quality, indicating poor particle coalescence.

In Figure 6, which shows the WAXS patterns of 0.7 mm diameter struts, the peak of the stable phase, γ, starts to present an intensity higher than the metastable phase, γ_m. The WAXS patterns of 1.0 mm and 1.5 mm diameter struts are shown in Figure 7 and 8 respectively. The peak intensity corresponding to the γ phase is notoriously higher in the patterns corresponding to the 1.5 mm diameter struts. Moreover, the intensity of the γ phase keeps increasing as the sample size increases, as it is observed in Figure 9, which shows the WAXS patterns of the lattice with 1.0 mm diameter struts and the macroscopic bulk sample, where the pattern in Figure 9b presents the largest difference of intensities between γ and γ_m peaks, being γ peak the one with the highest intensity. The WAXS pattern that corresponds to the bulk sample is the most similar to the pattern of the melt with slow cooling (M.s) sample in Figure 4a, suggesting that among all additive manufactured samples, the bulk one presents the lowest volume fraction of unmelted or partially melted particles and the best coalescence quality between particles.

In addition, the absence of the mesomorphic γ' phase (Figure 4b) on the additively manufactured samples indicates that they have not been subjected to rapid cooling during the manufacturing process.

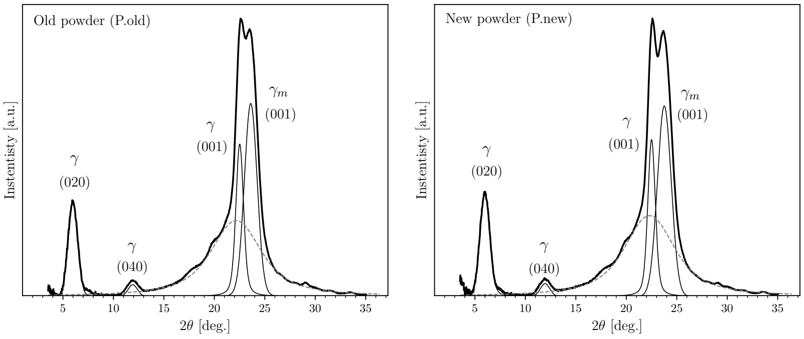

(a) **(b)**

Figure 3: Graphs presenting WAXS patterns, peak deconvolution and identification of the crystalline peaks and amorphous phase (discontinuous line) of a) old powders, b) new powders.

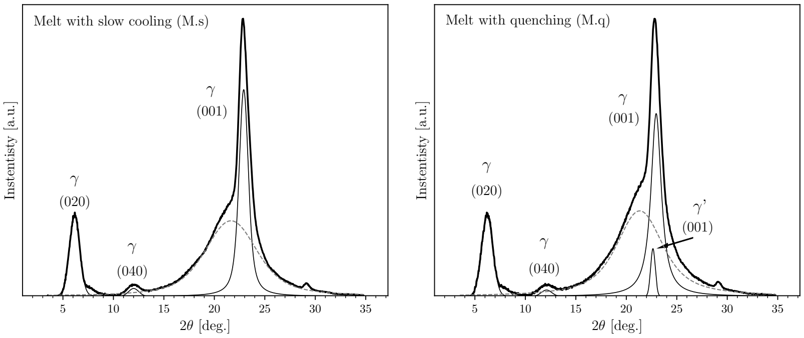

(a) **(b)**

Figure 4: Graphs presenting WAXS patterns, peak deconvolution and identification of the crystalline peaks and amorphous phase (discontinuous line) of the melts with a) slow cooling, b) quenching.

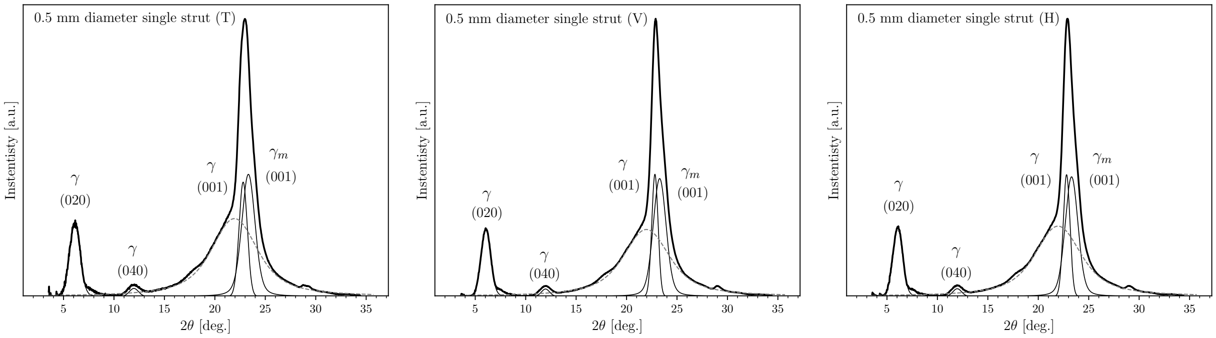

(a) **(b)** **(c)**

Figure 5: Graphs presenting WAXS patterns, peak deconvolution and identification of the crystalline peaks and amorphous phase (discontinuous line) of single struts of 0.5 mm diameter a) T, b) V, c) H.

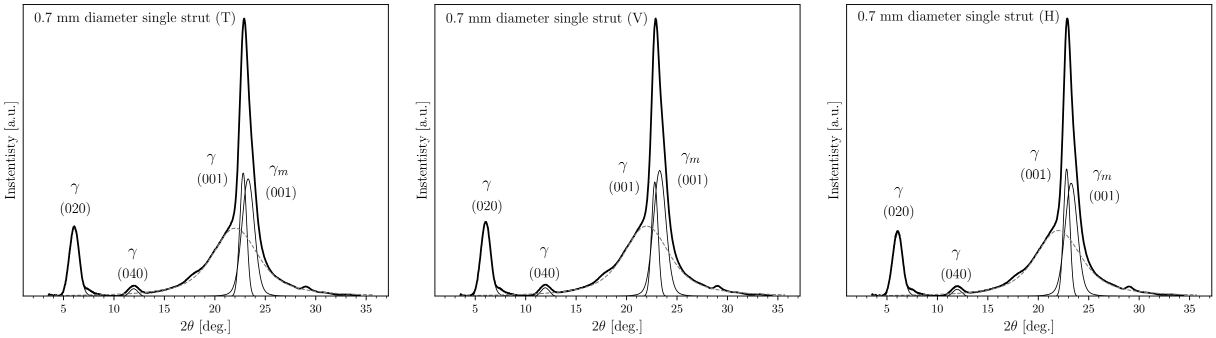

(a) **(b)** **(c)**

Figure 6: Graphs presenting WAXS patterns, peak deconvolution and identification of the crystalline peaks and amorphous phase (discontinuous line) of single struts of 0.7 mm diameter a) T, b) V, c) H.

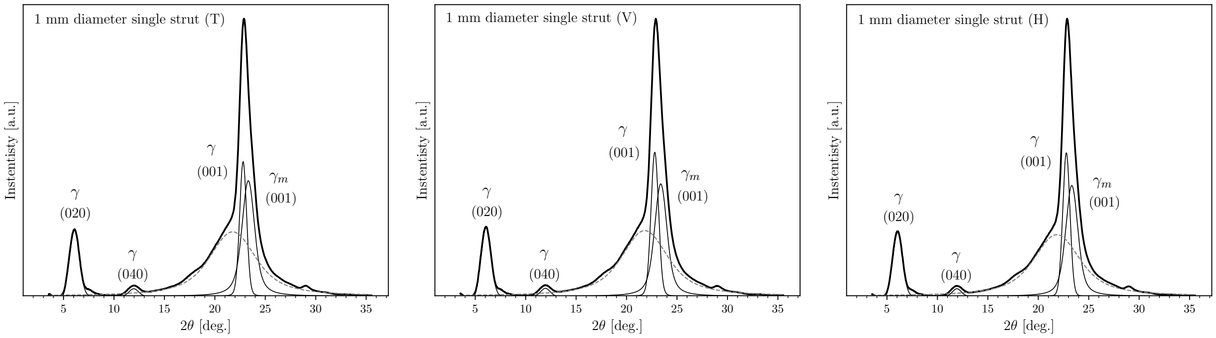

(a) **(b)** **(c)**

Figure 7: Graphs presenting WAXS patterns, peak deconvolution and identification of the crystalline peaks and amorphous phase (discontinuous line) of single struts of 1.0 mm diameter a) T, b) V, c) H.

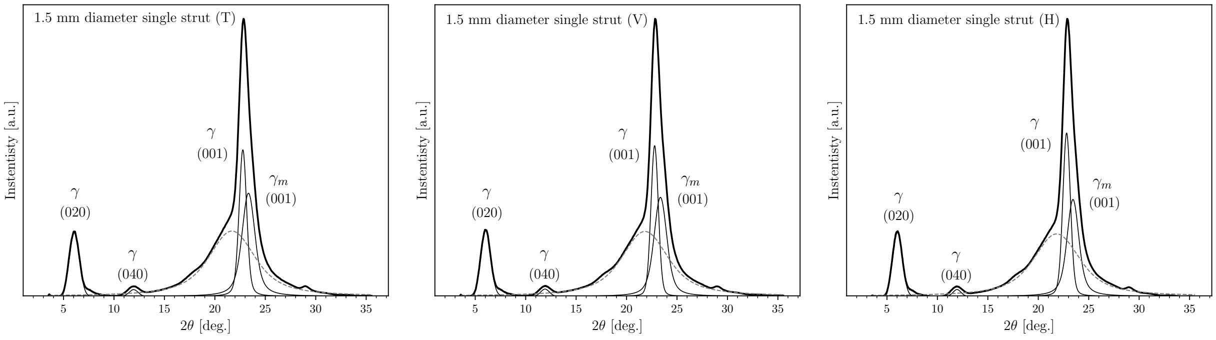

(a) **(b)** **(c)**

Figure 8: Graphs presenting WAXS patterns, peak deconvolution and identification of the crystalline peaks and amorphous phase (discontinuous line) of single struts of 1.5 mm diameter a) T, b) V, c) H.

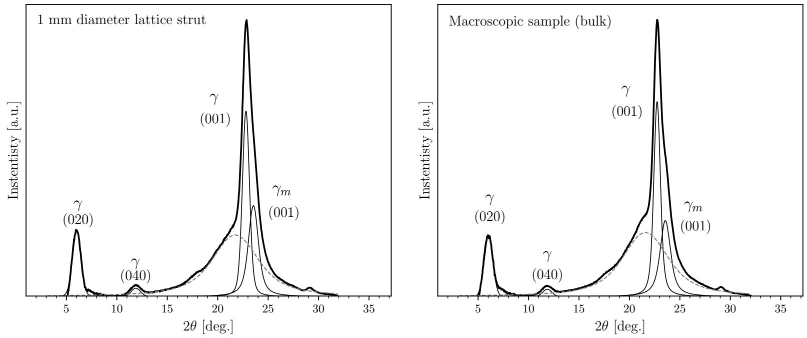

(a) **(b)**

Figure 9: Graphs presenting WAXS patterns, peak deconvolution and identification of the crystalline peaks and amorphous phase (discontinuous line) of a) 1 mm diameter lattice strut and b) bulk sample.